

Cirrus cloud thinning using a more physically-based ice microphysics scheme in the ECHAM-HAM GCM

Colin Tully , David Neubauer , Nadja Omanovic , and Ulrike Lohmann

Institute for Climate and Atmospheric Science, ETH Zurich, Zurich, Switzerland

Correspondence: Colin Tully (colin.tully@env.ethz.ch) or Ulrike Lohmann (ulrike.lohmann@env.ethz.ch)

Abstract. Cirrus cloud thinning (CCT) is a relatively new radiation management proposal to counteract anthropogenic climate warming by targeting Earth's terrestrial radiation balance. The efficacy of this method was presented in several general circulation model (GCM) studies that showed widely varied radiative responses, originating in part from the differences in the representation of cirrus ice microphysics between the different GCMs. The recent implementation of a new, more physically-based ice microphysics scheme (Predicted Particle Properties, P3) that abandons ice hydrometeor size class separation into the ECHAM-HAM GCM, coupled to a new approach for calculating cloud fractions that increases the relative humidity (RH) thresholds for cirrus cloud formation, motivated a reassessment of CCT efficacy. In this study, we first compared CCT sensitivity between the new cloud fraction approach and the original ECHAM-HAM cloud fraction approach. With Consistent with previous approaches using ECHAM-HAM, with the P3 scheme and the higher RH thresholds for cirrus cloud formation, we ~~do not~~ find a significant cooling response ~~of -0.36 Wm^{-2} only for our simulation with a seeding particle concentration of 1 L^{-1} , due mostly to rapid cloud adjustments~~ in any of our simulations. The most notable response from our extreme case is the reduction of the maximum global-mean net top-of-atmosphere (TOA) radiative anomalies from overseeding by more than 50 %, from 9.0 Wm^{-2} with the original cloud fraction approach, down to 4.3 Wm^{-2} using the new cloud fraction RH thresholds by avoiding artificial ice-cloud expansion upon ice nucleation. Even with this reduction with the updated cloud fraction approach, the TOA anomalies far exceed those reported in previous studies. We attribute the large positive TOA anomalies to seeding particles overtaking both homogeneous nucleation and heterogeneous nucleation on mineral dust particles within cirrus clouds to produce more numerous and smaller ice crystals. This effect is amplified by longer ice residence times in clouds due to the ~~more realistic~~, slower removal of ice via sedimentation in the P3 scheme. In an effort to avoid this overtaking effect of seeding particles, we increased the default critical ice saturation ratio ($S_{i,\text{seed}}$) for ice nucleation on seeding particles from the default value of 1.05 to 1.35 in a second sensitivity test. With the higher $S_{i,\text{seed}}$ we ~~eliminate overseeding and are able to produce cooling responses over a broader range of seeding particle concentrations, with the largest cooling of -0.32 Wm^{-2} for a seeding particle concentration of 10 L^{-1} , drastically reduce overseeding~~, which suggests that $S_{i,\text{seed}}$ is a key factor to consider for future CCT studies. However, the global-mean TOA anomalies contain high uncertainty. In response, we examined the TOA responses regionally and found that specific regions only show a small potential for targeted CCT, which is partially enhanced by using the larger $S_{i,\text{seed}}$. Finally, in a seasonal analysis of TOA responses to CCT, we find that our results do not ~~support confirm~~ the previous finding that high-latitude wintertime seeding is a feasible strategy to enhance CCT efficacy, as seeding in our model enhances the already positive cirrus longwave cloud radiative effect ~~. Instead our results show that~~

~~summertime cooling occurs due to adjustments of~~ for most of our simulations. Our results also show feedbacks on lower-lying mixed-phase and liquid clouds ~~through the reduction of ice crystal sedimentation that reduces cloud droplet depletion and~~ results in stronger cloud albedo effects. However, this is outweighed by stronger longwave trapping from cirrus clouds with more numerous and smaller ice crystals. Therefore, we conclude that CCT is unlikely to act as a feasible climate intervention strategy on a global scale, ~~and should be investigated further with higher-resolution studies in potential target regions and with studies dedicated to assessing potentially realistic seeding particle materials.~~

Copyright statement.

35 1 Introduction

Limiting 21st ~~Century~~ century global average warming to within 2 °C, following the 2015 Paris Climate Agreement, through greenhouse gas emissions reduction alone remains a highly ambitious goal. Amid growing concern of this infeasibility, several climate intervention (CI, also referred to as climate engineering or geoengineering) methods were proposed as potential mitigation strategies in order to limit future warming (Vaughan and Lenton, 2011). CI strategies encompass carbon sequestration, 40 which targets one of the main drivers of anthropogenic climate change, namely increased atmospheric CO₂ concentrations, and radiation management (RM), which indirectly counteracts warming by altering Earth's radiation balance. These RM schemes can be further divided between solar, shortwave (SW) and terrestrial, longwave (LW) radiation strategies. The focus of this study is on one particular LW radiation strategy, cirrus cloud thinning (CCT), also referred to as cirrus seeding, that aims to increase the amount of outgoing LW radiation to space by altering the formation pathways of cirrus clouds using artificial ice 45 nucleating particles (INPs).

Cirrus clouds are found in the upper troposphere at temperatures below 238 K (cirrus regime) and as such consist entirely of ~~ice crystals~~ ice crystals (ICs). Unlike their lower-altitude mixed-phase or liquid counterparts, cirrus clouds possess a relatively weak SW albedo effect while significantly modulating outgoing LW radiation. They absorb LW radiation emitted at warmer temperatures from Earth's surface and the lower-lying atmosphere, and re-emit it at ~~low~~ their lower temperatures, resulting 50 in a top-of-atmosphere (TOA) "trapping" effect that warms the atmosphere below (Hong et al., 2016; Gasparini et al., 2020). However, the magnitude of this cirrus cloud radiative effect (CRE) ~~of cirrus clouds~~ is strongly influenced by the microphysical properties of the clouds ~~(e.g. the ice crystal number concentration (ICNC) and their sizes, which ice crystal sizes), which~~ in turn are determined by the ice formation pathways (Stephens et al., 1990; DeMott et al., 2003, 2010; Krämer et al., 2016; Heymsfield et al., 2017).

55 Ice formation in cirrus occurs via two modes: homogeneous and heterogeneous nucleation. The former occurs as the spontaneous freezing of aqueous solution droplets at a relative humidity with respect to ice between 150 % and 170 % (Koop et al., 2000; Kärcher and Lohmann, 2002; Heymsfield et al., 2017) in the absence of a surface for ice nucleation. Due to the stochastic nature of a homogeneous nucleation event, numerous ice particles can form (Krämer et al., 2016; Heymsfield et al., 2017;

Gasparini et al., 2018) that are limited in size due to their competition for the available water vapor (Ickes et al., 2015). The
60 resulting cirrus ICNC, however, is sensitive to the appropriate conditions, namely the updraft speed that determines the magni-
tude of ice supersaturation (Kärcher and Lohmann, 2002; Lohmann and Kärcher, 2002; Kärcher et al., 2006; Kuebbeler et al.,
2014; Jensen et al., 2016b).

Heterogeneous ice nucleation occurs on the surface of a solid aerosol particle called an INP. The availability of the INP
surface lowers the energy barrier for ice germ formation, allowing ice nucleation at lower ice supersaturations and higher tem-
65 peratures than homogeneous freezing. However, understanding how heterogeneous nucleation impacts cirrus cloud properties
is complicated by the fact that several mechanisms exist for ice formation via an INP (Heymsfield et al., 2017). Plus, only a
small fraction of aerosols acts as INPs, which are even more sparsely populated in the upper troposphere, with limited mea-
surements in the cirrus regime (DeMott et al., 2003, 2010; Cziczo et al., 2013). Significant research continues on the ability of
various materials (e.g. mineral dust (Möhler et al., 2008; Lohmann et al., 2008; Murray et al., 2012; Ullrich et al., 2017), and
70 aircraft soot (Mahrt et al., 2018, 2020; Lohmann et al., 2020)) to act as INPs (Kanji et al., 2017).

The differences in the ice formation pathways via the two nucleation modes can result in cirrus clouds with different prop-
erties (Krämer et al., 2016; Heymsfield et al., 2017; Gasparini et al., 2018). While homogeneous nucleation tends to form
numerous small ~~ice crystals~~ ICs, the number of ice particles formed by heterogeneous nucleation is dependent on the availabil-
ity of INPs, especially in the case of slow updrafts (Kärcher and Lohmann, 2003; Spichtinger and Cziczo, 2010). In the case
75 of stronger updrafts or in an environment with a low INP concentration, heterogeneous nucleation ~~is less effective as water
vapor consumption~~ may not be sufficient to ~~diminish the updraft-fueled supersaturation increase~~ deplete the excess water vapor
so that homogeneous nucleation occurs in addition (DeMott et al., 2010; Jensen et al., 2016b). Krämer et al. (2016) and Gas-
parini et al. (2018) reported noticeable differences in the ice water content (IWC) of cirrus formed directly from the gas phase
("in-situ") via the two nucleation modes, with heterogeneously-formed cirrus associated with having lower IWC and smaller
80 ICNC than homogeneously-formed cirrus. Differences are also evident in ice particle sizes, which are indirectly related to the
ICNC, with fewer ~~particles being larger~~, larger particles in heterogeneously-formed cirrus than numerous small particles in
homogeneously-formed cirrus (Heymsfield et al., 2017). DeMott et al. (2010) found that the smaller ice particles formed by
homogeneous nucleation form cirrus clouds at higher altitudes (i.e. colder temperatures), contributing to a stronger warming
effect. The fewer and larger ice particles formed on INPs result in lower and warmer cirrus that have a weaker warming effect.
85 The differences in radiative effects between the ice nucleation modes was also assessed by Lohmann et al. (2008) with the
ECHAM general circulation model (GCM). In a series of sensitivity tests they found that switching cirrus ice nucleation from
homogeneous only to purely heterogeneous nucleation reduced the net cloud radiative forcing by roughly 2 Wm^{-2} . A similar
response was found when a simplified simulation of competition between the two nucleation modes in the cirrus regime was in-
cluded. The responses can be explained through changes in ice crystal fall speeds, which are closely related to nucleation rates
90 that determine the initial size of the ~~ice crystals~~ ICs (Mitchell et al., 2008). Following these findings, Mitchell and Finnegan
(2009) were the first to propose using efficient artificial INPs (i.e. "seeding particles") to alter cirrus ice environments away
from small ice particles formed via homogeneous nucleation to predominantly larger ice particles formed via heterogeneous
nucleation that sediment quicker and reduce cirrus cloud lifetimes, following a process coined as the negative Twomey effect

(Kärcher and Lohmann, 2003). In the preliminary analysis by Mitchell and Finnegan (2009), they proposed CCT could have a
95 cooling potential of ~~more than about~~ -2.8 Wm^{-2} that could noticeably counteract warming from a doubling of CO_2 .

Natural nucleation competition in cirrus was excluded in the first ~~GCM study~~ dedicated modeling study of CCT by Storelvmo
et al. (2013), who assumed all cirrus formed via homogeneous nucleation in the CAM5 general circulation model (GCM).
Globally uniform seeding produced a maximum negative net ΔCRE around -2.0 Wm^{-2} , corresponding to optically thinner
cirrus with an average ice crystal effective radius increase of $4 \mu\text{m}$ and decrease of ICNC by more than 250 L^{-1} . Of note from
100 their study was evidence of an optimal seeding particle concentration around 18 L^{-1} , below which the seeding particles were
ineffective due to insufficient water vapor consumption. However, a seeding concentration above the optimal concentration led
to "overseeding", whereby the numerous seeding INPs formed smaller ice particles that elongated cirrus lifetimes and exerted
a warming effect (Storelvmo et al., 2013).

The assumption that cirrus form primarily by homogeneous nucleation was challenged when Cziczo et al. (2013) observed
105 heterogeneous nucleation as the dominant source of cirrus ice over North and Central America. To account for the uncertainty
surrounding the dominant ice nucleation mode in cirrus, Storelvmo and Herger (2014) conducted several seeding simula-
tions with different configurations of ice nucleation competition, including different concentrations of background dust as
active INPs. They found a reduced CRE response up to -2 Wm^{-2} in their simulations where seeding particles were added to
homogeneous-heterogeneous nucleation competition and homogeneous-only configurations, with an optimal seeding particle
110 concentration of 18 L^{-1} as in Storelvmo et al. (2013). Additionally, they found that seeding at this optimal concentration in
their model led to optically thinner clouds that contained a weaker overall SW CRE (i.e. reduced albedo), allowing more SW
to reach the surface. However, this effect was outweighed by the reduction in cirrus LW CRE (i.e. reduced LW "trapping"). To
some extent, this finding is in line with the latest compilation of in-situ observations of unseeded cirrus by Krämer et al. (2020),
who found that optically thicker, liquid-origin τ -cirrus (cloud optical depth, $\tau > 1$) tend to have a strong cooling effect due to
115 a higher albedo, whereas optically thinner, in-situ origin τ -cirrus ($\tau < 1$) have a large warming effect in response to a weaker
albedo and a larger LW-trapping potential (i.e. cooler temperatures) that peaks with τ between 0.4 and 0.5. Krämer et al.
(2020) further divide in-situ origin cirrus between fast and slow updrafts, with the latter having a stronger warming potential
than the former. As CCT targets the slower updraft cirrus, due to weaker dynamic forcing (Gasparini et al., 2017; Krämer et al.,
2016; Krämer et al., 2020), thinning these cirrus weakens their warming potential. Therefore, reducing the optical thickness
120 of these latter cirrus through seeding, like in Storelvmo and Herger (2014), not only reduces their already weak SW CRE, but
reduces their LW CRE more effectively. At higher seeding particle concentrations and for their heterogeneous-only simula-
tion, Storelvmo and Herger (2014) found warming of more than 1.0 Wm^{-2} as a result of overseeding. They also showed that
non-uniform seeding of only 40 % or 15 % of the globe, to avoid ineffective regions like the tropics, has a cooling potential
similar to their uniform cases due to a lack of cirrus SW radiative effect at higher latitudes in winter and a reduced natural
125 background aerosol loading. Seeding a smaller area around 15 % of the globe in winter resulted in a similar ΔCRE response of
 -2.1 Wm^{-2} , through mostly LW cloud forcing reduction while avoiding large compensating SW forcing increases (Storelvmo
et al., 2014). Similarly, Gruber et al. (2019) simulated CCT using the higher-resolution ICON-ART model in a small ~~Arctic~~
region region in the Arctic centered over Greenland. They also found large negative TOA LW anomalies from seeding, but

only in their simulations where background mineral dust concentrations were limited. The CCT cooling potential decreased in
130 their simulations with increasing background mineral dust concentrations.

Penner et al. (2015) re-evaluated the results by Storelvmo et al. (2013), Storelvmo and Herger (2014), and Storelvmo et al.
(2014) using an updated version of CAM5 that not only included the cirrus ice nucleation competition between homogeneous
and heterogeneous nucleation, but also accounted for the consumption of water vapor by pre-existing ice transported into
the cirrus regime. Additional updates were made to the dynamical environment to allow higher updraft velocities for the
135 cirrus ice nucleation scheme, and to the aerosol environment to include secondary organic aerosols (SOAs) as potential INPs.
Only their seeding simulation with no pre-existing ice, no SOAs acting as INPs, and a limited updraft velocity showed any
significant net negative TOA forcing up to -0.74 W m^{-2} in a similar optimal seeding particle concentration range as [found by](#)
Storelvmo et al. (2013). All other simulations that included higher concentrations of INPs and higher updraft velocities resulted
in positive net forcings. Gasparini and Lohmann (2016) extended these results using the ECHAM-HAM GCM with a cirrus
140 ice nucleation scheme that also considered the competition between homogeneous and heterogeneous nucleation, and water
vapor consumption on pre-existing ice (Kärcher et al., 2006; Kuebbeler et al., 2014). Like Storelvmo et al. (2013), Storelvmo
and Herger (2014), and Penner et al. (2015), Gasparini and Lohmann (2016) reported an optimal seeding particle concentration
~~that was of 1 L^{-1}~~ , an order of magnitude lower than previous studies ~~at 1 L^{-1}~~ . The maximum net TOA negative forcing in their
full nucleation competition setup with the optimal seeding particle concentration was -0.25 W m^{-2} , which was also smaller
145 than in previous studies. Seeding with more than 1 L^{-1} resulted in warming from overseeding, which could be limited by the
presence of pre-existing ice particles. However, in all of their simulations the net TOA responses contained high uncertainty.

Overall, the more positive forcing responses presented by Gasparini and Lohmann (2016) were attributed to a decrease in the
average size of ~~ice crystals (ICs)~~ ICs post-seeding, and an increase in cirrus coverage in previously clear-sky areas, a potential
side effect of seeding presented by Mitchell and Finnegan (2009). The efficiency of the seeding particles to consume water
150 vapor was cited as the cause of the observed IC response, and as they highlight points to the dominance of heterogeneous
nucleation to [background](#) cirrus formation in ECHAM-HAM. A source attribution analysis revealed that most cirrus formed
via heterogeneous nucleation at a typical altitude of 200 hPa, even in high latitude regions (Gasparini and Lohmann, 2016),
contrasting previous studies by Storelvmo et al. (2013), Storelvmo and Herger (2014), and Penner et al. (2015). This difference
between the nucleation mode dominance in different model setups is further evaluated in Gasparini et al. (2020), where even
155 without seeding the global mean cirrus CRE is 2.0 W m^{-2} greater in CAM5 than in ECHAM. With more heterogeneous
nucleation present in cirrus in ECHAM-HAM, it is less sensitive to seeding and has a much lower optimal seeding particle
concentration than CAM5 (Gasparini et al., 2020). Overseeding can therefore occur more readily as water vapor consumption
affects more particles.

Unintended side effects are likely with any climate intervention strategy. For example, a widely studied solar radiation
160 management strategy, stratospheric aerosol injection, aims to increase planetary albedo by mimicking natural sulphur aerosol
perturbations from volcanoes (Robock, 2000; Crutzen, 2006). However, numerous studies found that injecting such particles
into the stratosphere may deplete ozone and reduce the efficacy of renewable energy production (Crutzen, 2006; Robock et al.,
2008; Murphy, 2009; Vaughan and Lenton, 2011). Alternatives to sulphur particles, like calcite, were investigated and found

to lead to increased stratospheric ozone (Dykema et al., 2016; Keith et al., 2016), ~~though using such particles~~. [Stratospheric aerosol injection](#) may also impact cirrus clouds ([Cziczo et al., 2019](#)) ([Kuebbeler et al., 2012](#); [Cziczo et al., 2019](#)). In summary, assessing the potential side effects of any climate intervention strategy is crucial in order to understand future implementation.

To date, assessing the climate impact of CCT is limited to global or regional modeling studies that require a comprehensive understanding of the complex ice processes occurring in cirrus. With different approaches employed in each model, the climate impact of CCT, including any unintended side effects, remains uncertain, which highlights the need for a consistent, physically-based approach to simulating the complex [microphysical](#) processes governing ice formation and growth in cirrus clouds (Gasparini et al., 2020). In this study, we investigate the climate impact of CCT using a new ice microphysics scheme in the ECHAM-HAM GCM that includes a prognostic treatment of ice sedimentation by introducing a single ice category, and an updated approach for calculating ice cloud fractions that allows for fractional cirrus gridbox coverage ([Section 2](#) [Section 2](#)). We perform CCT simulations using a cirrus ice nucleation scheme that accounts for the competition between homogeneous and heterogeneous nucleation, and depositional growth onto pre-existing ice particles ([Section 2](#) [Section 2](#)). Additional ice source number and mass mixing ratio tracers are implemented to directly investigate the impacts of seeding on the competition between the different ice nucleation modes. Results are presented in [Section 3](#) [Section 3](#), followed by a discussion of our findings in [Section 4](#). [Section 4](#). We present our conclusions in [Section 5](#). [Section 5](#).

2 Methods

2.1 Model Description

We conduct our seeding experiments using the ECHAM6.3-HAM2.3 aerosol-climate GCM (Stier et al., 2005; Zhang et al., 2012; Stevens et al., 2013; Neubauer et al., 2019; Tegen et al., 2019). We use the horizontal resolution T63 ($1.875^\circ \times 1.875^\circ$), with 47 vertical levels (L47) up to 0.01 hPa, which corresponds to a vertical resolution of around 1 km in the upper troposphere at cirrus altitudes. The model timestep is 7.5 minutes.

The two-moment ice microphysics scheme by Lohmann et al. (2007), used in the default version of ECHAM6.3-HAM2.3, was succeeded by the Predicted bulk Particle Properties (P3) scheme by Morrison and Milbrandt (2015) that was ported to ECHAM-HAM by Dietlicher et al. (2018, 2019). It replaces an earlier method of artificially separating ice particles into different size classes (Levkov et al., 1992), rendering the use of the tuning parameter for the rate of snow formation unnecessary (Dietlicher et al., 2019). Instead, ice is represented with a single prognostic category based on mass-to-size relationships. With the single ice category no longer differentiating between in-cloud and precipitating ice, vertical advection and precipitation processes were also updated to include a substepping approach for prognostically solving ice sedimentation. This allows for sedimenting ice to be subjected to cloud processes as it falls, and for numerical stability within the cloud scheme (Dietlicher et al., 2018). For more specific information on P3 and its implementation within ECHAM6, please refer to Dietlicher et al. (2018, 2019).

A separate cirrus nucleation scheme by Kärcher et al. (2006) that was adapted for ~~the~~ ECHAM-HAM by Kuebbeler et al. (2014) handles in-situ ice nucleation within cirrus clouds. It simulates the competition for water vapor between heterogeneous

and homogeneous nucleation, and between depositional growth onto ~~pre-existing~~ pre-existing ice particles that are transported into the cirrus regime from deep convective detrainment or from stratiform mixed-phase clouds. The scheme ~~is based on~~ uses a sub-stepping approach to simulate the temporal evolution of ice saturation ~~through the~~ during the formation-stage of a cirrus cloud. This is achieved by calculating the balance between the adiabatic cooling of rising air, with the associated saturation increase, and the diffusional growth of ice particles that consume the available water vapor. The ~~adiabatic~~ cooling rate is determined by the vertical velocity, which is represented by a grid-mean value plus a turbulent component based on the turbulent kinetic energy (TKE), (Kuebbeler et al., 2014). Orographic effects on vertical velocity as well as small-scale gravity waves (~~Kärcher et al., 2006; Joos et al., 2010; Jensen et al., 2016a~~) (Kärcher et al., 2006; Joos et al., 2008, 2010; Jensen et al., 2016a) in the upper troposphere are not included in this study. We provide a short analysis that verifies our model without orographic effects in Appendix A. In summary, by using the new P3 ice microphysics and the updated cirrus ice nucleation schemes, including orographic effects acts to drastically increase cirrus ICNC while reducing spatial heterogeneity. As the magnitude of the ~~saturation ratio in the updraft is related to~~ ice saturation ratio is determined only by the vertical velocity, a fictitious downdraft is introduced at the end of each timestep of the cirrus scheme to quantify the ~~saturation ratio decrease by~~ effect of water vapor consumption ~~onto ice~~ (~~Kuebbeler et al., 2014~~) during new ice formation events or onto pre-existing ice particles (Kuebbeler et al., 2014). The updated vertical velocity therefore determines the evolution of the ice saturation ratio in subsequent sub-timesteps. Muench and Lohmann (2020) updated the water vapor consumption by ice, following the diffusional growth equation (Lohmann et al., 2016). The temporal change of the saturation ratio follows such that if the updraft is stronger than the water vapor consumption by pre-existing ice and heterogeneous INPs, then it may reach a suitable magnitude for homogeneous nucleation to occur. The opposite is true in weaker updraft regimes or in high INP concentration environments (Kärcher et al., 2006). ~~A sub-time-stepping approach is employed~~ The sub-stepping approach in the cirrus scheme ~~to simulate the rise of the air parcel and the subsequent saturation ratio decrease by ice formation, whereby the entire temporal evolution of the saturation ratio is simulated within a single model timestep~~ is computed dynamically based on a 1% rate of change of the ice saturation ratio between each sub-timestep.

To simulate the competition between homogeneous and heterogeneous nucleation, several freezing modes are introduced into the cirrus scheme (Table 1), including pre-existing ice. In general, the cirrus nucleation scheme follows an "energy-barrier" approach, with pre-existing ice and the most efficient INP, dust (in the default setup), consuming water vapor at a lower ice saturation ratio (S_i). An ice formation event in each mode can occur as either a threshold freezing process or as a continuous freezing process (Muench and Lohmann, 2020). The former is based on the original cirrus scheme by Kärcher et al. (2006), whereby ice forms by a particular mode when its critical ice saturation ratio ($S_{i,crit}$) is reached. In our setup, homogeneous nucleation of liquid-sulphate aerosols with a temperature-dependent $S_{i,crit}$ between 1.4 and roughly 1.75 (Koop et al., 2000), and immersion freezing of soluble material coated dust with a $S_{i,crit}$ of 1.3, act as threshold freezing modes. As a threshold process, all aerosol particles associated with the mode form ice that proceeds to deplete available water vapor and reduce S_i . For dust immersion freezing, only 5% of the total dust aerosol concentration from the aerosol module, HAM, act as INPs within the mode, following Gasparini and Lohmann (2016). Muench and Lohmann (2020) introduced the latter, continuous freezing process to account for the saturation-dependent activated fraction (AF) of INPs available for heterogeneous nucleation. We

Table 1. Summary of the different aerosol species available for in-situ ice nucleation within the cirrus scheme, including information on the average radius of the particles, the critical ice saturation ratio above which these particles will nucleate ice, the freezing mechanism by which nucleation will occur, and the freezing method within the context of the cirrus scheme following Muench and Lohmann (2020).

<u>Particle type</u>	<u>Mean radius (μm)</u>	<u>Critical S_i</u>	<u>Freezing mechanism</u>	<u>Freezing method</u>
Insoluble dust	0.05 to 0.5 > 0.5	Temperature-dependent, but > 1.1 Temperature-dependent, but > 1.2	Deposition nucleation	Continuous
<u>Soluble dust</u>	<u>> 0.05</u>	<u>1.3</u>	<u>Immersion freezing</u>	<u>Threshold</u>
<u>Aqueous sulfate</u>	<u>All size modes: < 0.005 to > 0.5</u>	<u>1.4</u>	<u>Homogeneous nucleation</u>	<u>Threshold</u>

include deposition on insoluble accumulation and coarse size mode (Stier et al., 2005; Zhang et al., 2012; Tegen et al., 2019) dust particles as continuous freezing modes. The AF is calculated using a temperature-dependent $S_{i,\text{crit}}$ threshold of 1.2 for $T > 220$ K, and 1.1 for $T \leq 220$ K based on laboratory measurements by Möhler et al. (2006). At every timestep in the cirrus
 235 scheme, the AF of these modes is calculated, and if ice forms it is added to the ice concentration.

~~In this study, we introduce two significant improvements to the representation of the continuous freezing modes. Firstly, we implement a budgeting approach for the available dust that was not previously included in the latest version of the cirrus scheme. This reduces the potential to over-predict the amount of ice that forms heterogeneously through deposition onto dust particles. Secondly, we introduce the differential approach by Kärcher and Marcolli (2021) that further addresses the
 240 over-prediction issue associated with heterogeneous nucleation on dust when using an INP budgeting approach. In this new approach we no longer use the cumulative of the current cirrus-model time-step based on the current . Instead, only if the cumulative of the current cirrus-model time-step is greater than the previous step is the differential calculated as the difference between the cumulative of the current cirrus-model time-step and the previous cirrus-model time-step cumulative. As a short conceptual example, if in the first cirrus-model time-step the cumulative = 5% and in the second cirrus-model time-step the
 245 cumulative = 10%, the differential for the second cirrus-model time-step would be 5%. This has the potential to drastically reduce the amount of heterogeneous nucleation on dust particles, and may have wider implications on efficacy, not considered in previous studies (Gasparini and Lohmann, 2016; Gasparini et al., 2017, 2020).~~

Following Gasparini and Lohmann (2016), we introduce seeding particles as a separate threshold freezing mode into the cirrus scheme for temperatures below 238 K, increasing the competition for available water vapor. All seeding particles can
 250 nucleate ice with a $S_{i,\text{crit}}$ (hereafter seeding particle critical saturation ratio ($S_{i,\text{seed}}$)) of 1.05 (Storelvmo and Herger, 2014), and later with $S_{i,\text{seed}} = 1.35$ ([below Section 2.2](#)). The seeding particles have a modal radius of $0.5 \mu\text{m}$ like in Gasparini and Lohmann (2016). We perform uniform global seeding with no spatial or temporal variability in seeding particle concentration for comparability with previous GCM studies, except for an altitude restriction below 100 hPa to minimize seeding of the stratosphere. This seeding restriction to altitude levels below 100 hPa (i.e. higher pressure levels) is in line with proposed
 255 real-world delivery mechanisms for seeding particles with commercial aircraft (Mitchell and Finnegan, 2009).

Cloud cover is based on the diagnostic approach by Sundqvist et al. (1989), (~~hereafter referred to as S89~~), that assumes fractional cloud formation exists due to relative humidity (RH) variability within the gridbox. The formulation was developed for liquid (warm) clouds, using a critical RH (RH_{crit}) above which fractional cloud cover in a gridbox can occur. Full grid-box coverage occurs when grid-mean RH reaches 100 % with respect to liquid water. This formulation works well for warm clouds, but as Kuebbeler et al. (2014) and Dietlicher et al. (2018, 2019) note, it breaks down for mixed-phase clouds ($T < 273$ K) that may or may not include ice, presenting a difficult choice between RH with respect to liquid (RH_l) or ice (RH_i) ~~for full gridbox coverage to determine cloud fraction~~. The S89 approach for pure ice clouds ($T < 235$ K) is analogous to warm clouds in earlier versions of our model, where instead of liquid water saturation, full ~~gridbox~~ coverage occurs at ice saturation. As Kuebbeler et al. (2014) explain, when accounting for the ice supersaturation required for homogeneous or heterogeneous nucleation, this leads to full gridbox coverage of freshly nucleated cirrus clouds, an inconsistency between cloud fraction and the microphysics scheme (Kärcher and Burkhardt, 2008). This also may explain the high cirrus CRE in ECHAM6 found by Gasparini and Lohmann (2016). Dietlicher et al. (2019) updated the cloud fraction formulation for pure ice clouds to differ from liquid clouds by updating the RH ~~bounds conditions~~ in which an ice cloud can ~~form~~. ~~In our version of the model for this study, fractional ice cloud coverage no longer exists below ice saturation (i.e. $RH_{crit} = 100\% RH_i$, partially cover a gridbox. In this new scheme (hereafter, D19) that we use in this study, ice saturation ($S_i = 1.0$) , with full coverage following the Koop et al. (2000) is set as the lower boundary condition for partial ice cloud fractions. The upper boundary condition for full gridbox coverage for ice clouds is set following the theory for homogeneous nucleation of solution droplets by Koop et al. (2000). The difference between the two schemes is illustrated in Figure 1 that was adapted from Dietlicher et al. (2019). Both approaches use saturation adjustment to calculate ice cloud fractions, but D19 increases the bounds for ice cloud formation to allow for ice supersaturation, which is more realistic than the S89 approach that does not allow for ice supersaturation. For example with . As a contextual example, if ice were to form at ~~218 K-233 K~~ in an environment with $S_i = 1.612$, then D19 would adjust the supersaturation to that for aqueous solution droplets following Koop et al. (2000) to form a cirrus cloud that would fully cover the gridbox. calculate an ice cloud fraction < 1.0 , whereas S89 works in the same way, but instead would adjust the supersaturation ~~ice supersaturation down~~ to ice saturation ($= 1.0$) and also ~~and~~ would produce a fully covered gridbox ~~cloud fraction of 1.0~~.~~

Additional ice number and mass mixing ratio tracers were added to the model, following Dietlicher et al. (2019), to trace the origin of in-situ cirrus ice directly. We include two tracers for ice from homogeneous and heterogeneous nucleation, with additional tracers for heterogeneously-formed ice on dust and seeding particles, the sum of which equates to the total in-situ heterogeneously-nucleated ice tracer. The implementation of these tracers highlighted ~~erroneous scaling of the aerosol concentrations of the various freezing modes in the cirrus ice nucleation competition scheme an error when accounting for the number of aerosols that previously nucleated ice. The aerosol concentration of each freezing mode of the cirrus scheme was scaled~~ by the total amount of pre-existing ice. This ~~was updated to properly account approach overestimated the concentrations of in-cloud aerosols and underestimated the interstitial aerosol concentration. We updated the scaling of each aerosol concentration mode to account for~~ the fraction of each mode ~~of the out of the total~~ pre-existing ice ~~, excluding the dust deposition modes, which were updated with and the new differential (Kärcher and Mareolli, 2021) as detailed above~~ ~~concentration~~.

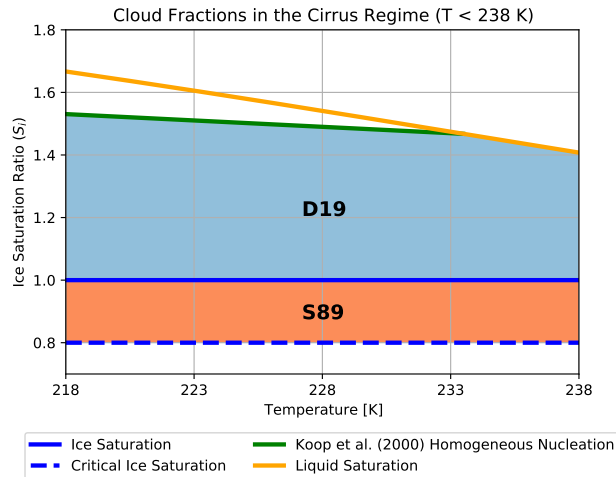


Figure 1. Cloud fraction schematic adapted from Dietlicher et al. (2019) showing the difference between the D19 and S89 approaches for calculating ice cloud fractions. The shaded areas show the temperature versus ice saturation ratio conditions where clouds can form, with the orange area for S89 and the blue area for D19. The blue line is the ice saturation line ($S_i = 1.0$), the blue dotted line is the critical ice saturation line for cloud formation in the S89 approach, the orange line is for liquid saturation with respect to ice saturation, and the green line is the homogeneous nucleation limit according to Koop et al. (2000).

These updates warranted a re-tuning of the model to primarily target the balance between global annual mean $\bar{\tau}$ -TOA SW and LW fluxes (Lohmann and Ferrachat, 2010; Mauritsen et al., 2012; Neubauer et al., 2019). A summary of the model configuration we utilize in this study compared to the "HET_CIR" simulation by Dietlicher et al. (2019) is presented in Table 2. Ice self-collection (~~eenislf~~) ~~was doubled to 6.0~~ γ_{isl} was increased from its original value in the base version of the model (Dietlicher et al., 2019) to ~~account for a too weak~~ 5.5 to account for too small TOA SW and LW fluxes. This adjustment strengthened both TOA fluxes, but the LW flux ~~was still~~ remained too weak. Therefore, to compensate, the auto-conversion rate from cloud liquid water to rain within convective cores was increased to ~~1.77~~. ~~As convective clouds also impact fluxes, we adjusted the auto-conversion~~ 1.75. In addition to radiative flux imbalance, we found that the model produced a global mean liquid water path (LWP) value that was beyond the upper value of the observations reported by Neubauer et al. (2019). To address this issue we halved the convective cloud mass-flux above the level of non-buoyancy (γ_{ctop}) to 0.1. As reducing this flux leads to more frequent and thicker boundary layer clouds (Mauritsen et al., 2012), we compensated this by increasing the autoconversion rate within stratiform liquid clouds (γ_r) to ~~2.48~~ 3 to maintain radiative balance. All other tuning parameters were kept the same as the "HET_CIR" configuration in Dietlicher et al. (2019). We also note a too negative net CRE after tuning, ~~which Dietlicher et al. (2019) attributed to a structural issue.~~ Dietlicher et al. (2019) state this points to a possible structural problem within the model. ~~In addition, our five-year global mean is 21.8 Wm^{-2} , which is weaker by about 0.2 Wm^{-2} than the lower range of the observations (Neubauer et al., 2019), which is related to the coarse vertical resolution that results in the under-prediction of low-level clouds (Pelucchi et al., 2021).~~

Table 2. Model configuration comparison between the "HET_CIR" simulation by Dietlicher et al. (2019) and our "Full_D19" reference simulation presented in this study. The tuning parameters include: ice self-collection (γ_{slf}), the autoconversion rate from cloud liquid water to rain within convective cores (γ_{cpr}), the convective cloud mass-flux above the level on non-buoyancy (γ_{ctop}), and the autoconversion rate within stratiform liquid clouds (γ_{r}).

<u>Parameter</u>	<u>HET_CIR</u>	<u>Full_D19</u>
<u>γ_{slf}</u>	<u>3.0</u>	<u>5.5</u>
<u>γ_{cpr}</u>	<u>1.5×10^{-4}</u>	<u>1.75×10^{-4}</u>
<u>γ_{ctop}</u>	<u>0.2</u>	<u>0.1</u>
<u>γ_{r}</u>	<u>4.4</u>	<u>8.3</u>

2.2 Experimental Setup

We performed cirrus seeding simulations using P3 with the cirrus scheme coupled to the new ~~fractional ice cloud cover~~
 310 ~~formulation ice-cloud fraction approach~~ (D19) described above. We examined seeding with full nucleation competition be-
 tween heterogeneous, homogeneous, and pre-existing ice. Additionally, we tested the original S89 ~~ECHAM6 ice cloud cover~~
~~ice-cloud fraction~~ approach (Stevens et al., 2013; Neubauer et al., 2014, 2019) within the framework of the P3 scheme (~~S89~~);
 we did not re-tune the model for simulations using S89 in order to examine the sensitivity of cirrus seeding to the ice cloud
 fraction scheme. Previous CCT studies include additional simulations in which they allow only homogeneous nucleation to
 315 occur in cirrus. Here, we chose to pursue full nucleation competition as a more realistic approach to examine the impact of
 seeding particles, mimicking a real-world implementation. For both model configurations (see Table 3) we implemented seed-
 ing ~~at every timestep particles~~ as an additional ~~heterogeneous~~ freezing mode in the cirrus ~~nucleation scheme such that only~~
~~ice-nucleation scheme continuously at every timestep, following on from previous approaches (i.e. without accounting for~~
~~those that already formed ice)~~. Only gridboxes that are ~~saturated-supersaturated~~ with respect to ice (i.e. $S_i \Rightarrow 1.0$) are seeded.
 320 We test four seeding INP concentrations of 0.1, 1, 10, and 100 INP L^{-1} to represent the spread of concentrations tested in
 previous studies (Storelvmo and Herger, 2014; Penner et al., 2015; Gasparini and Lohmann, 2016). Each simulation was ~~run~~
~~conducted~~ for five years between 2008 and 2012, inclusive, with three months of spin-up from 1st October 2007. Monthly
 mean sea surface temperatures and sea ice coverage are prescribed, and emissions are from the year 2010 following CMIP6
 methodology (van Marle et al., 2017; Hoesly et al., 2018).

325 The $S_{i,\text{seed}}$ of 1.05 follows Storelvmo and Herger (2014) and Gasparini and Lohmann (2016), and is based on suggestions of
 a potential seeding particle material, bismuth tri-iodide (BiI_3) (Mitchell and Finnegan, 2009). It is unclear whether this $S_{i,\text{seed}}$
 can be applied to a realistic seeding particle material. Therefore, to test the sensitivity of ice nucleation competition to the
 seeding INP, we ~~run~~ ~~conducted~~ additional seeding simulations with all seeding particle concentrations described above, with a
 $S_{i,\text{seed}}$ of 1.35 (Table 3). This ensures that seeding can occur in ice supersaturated environments below the lower homogeneous
 330 nucleation $S_{i,\text{crit}}$ threshold around 1.40 and above the maximum $S_{i,\text{crit}}$ for dust of 1.3.

Table 3. Experimental setup for cirrus seeding for the two ice-cloud fraction schemes. Both configurations include seeding particle concentrations of 0.1, 1, 10, and 100 L⁻¹. In addition, seeding is conducted for a seeding particle critical ice saturation ratio (S_i) of 1.05 and 1.35. The "Full" in the reference simulations refers to full ice nucleation competition between pre-existing ice, heterogeneous nucleation on mineral dust particles, and homogeneous nucleation of liquid sulfate aerosols in the in-situ cirrus scheme (Kärcher et al., 2006; Kuebbeler et al., 2014).

Ice-cloud fraction scheme	Description	Reference Simulation <u>simulation</u>	$S_{i,seed} = 1.05$	$S_{i,seed} = 1.35$
D19	new cloud fraction by Dietlicher et al. (2018, 2019)	Full_D19	Seed0.1 Seed1	Seed0.1_1.35 Seed1_1.35
S89	original cloud fraction by Sundqvist et al. (1989)	Full_S89	Seed10 Seed100	Seed10_1.35 Seed100_1.35

2.3 Uncertainty

We take particular care to quantify significance in our results, following the "false discovery rate (FDR)" method by Wilks (2016). The updated approach for conducting independent t-tests accounts for high spatial correlation of neighboring grid-points, i.e. the null hypothesis cannot ~~not~~ be as widely rejected when calculating significance. We calculate a 5% significance based on the inter-annual variability over the five years of simulation (~~Section 2.2~~ Section 2.2). The inter-annual variability is also used to calculate the 95 % confidence interval around the five-year mean.

3 Results

3.1 Model Validation

We start by evaluating the model with the new P3 ice microphysics scheme and the new D19 ice-cloud fraction approach for the unseeded reference case, by comparing ICNC data to the latest compilation of in-situ aircraft measurements by Krämer et al. (2016, 2020) in Figure 2. Model results represent the five-year mean temperature versus ICNC between 2008 and 2012. The observational data comprise multiple in-situ aircraft field campaigns between 1999 and 2017, totalling around 90 hours of flight data (Krämer et al., 2020), with different meteorological situations captured in the tropics, mid-latitudes, and the Arctic; southern high latitudes are not included. Although this is a much more significant compilation of observational data than was previously available, there remains a caveat that these data are not representative of the entire atmosphere (Krämer et al., 2020).

~~Model data are presented in a and the observations in b.~~ The median ICNC per temperature bin between 180 K and 250 K is also ~~plotted shown~~ for both data sets, with the observational median also ~~plotted presented~~ with the model data for comparison. Model-median ICNC values agree rather well with the observational median at temperatures between roughly ~~190 K and 230 K, and above 240 K~~ 205 K and 230 K. Between 230 K and 240 K the model-median diverges above the observational

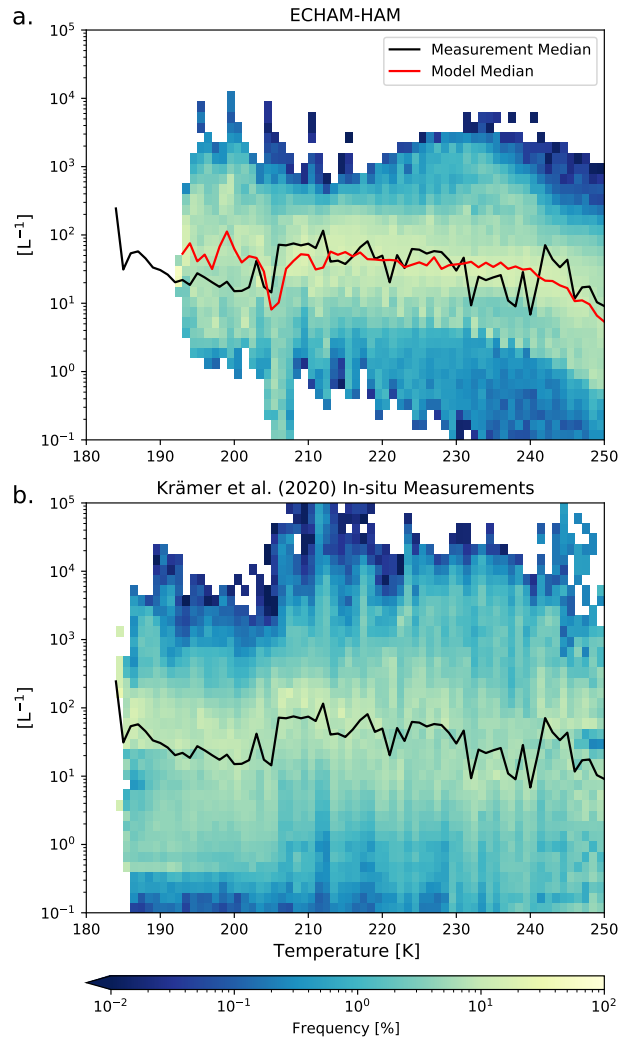


Figure 2. ICNC ($\text{in } \text{L}^{-1}$) frequency diagrams for ice crystals with a diameter of at least $3 \mu\text{m}$ as a function of temperature between 180 K and 250 K binned like in Krämer et al. (2020) for every 1 K. The five-year global mean data from the model is plotted in (a) and the compilation of in-situ flight data from Krämer et al. (2020) is plotted in (b). The red line in the upper plot represents the binned median ICNC value of the model data, and the black line in both plots is the same value for the observational data.

350 median where it does not capture the more frequent occurrence of lower ICNC values. Both the model and observations capture the tailing-off of ICNC at temperatures warmer than 240 K, with the model being slightly lower than the observations. ~~These phenomena~~ The small disagreements in these two temperature ranges may be linked to the default parameterization for heterogeneous nucleation on mineral dust particles in mixed-phase clouds in ECHAM ~~by Lohmann and Diehl (2006), which is based on dust immersion freezing rates. Villanueva et al. (2021).~~ The results by Villanueva et al. (2021) offer an explanation ~~in this regard. In their study, they~~ conducted several sensitivity tests with ECHAM-HAM using this default freezing rate-based

355 in this regard. In their study, they conducted several sensitivity tests with ECHAM-HAM using ~~this default freezing rate-based~~

~~scheme and an~~ the default rate-based immersion freezing scheme by Lohmann and Diehl (2006) and a newer AF approach based on dust particle surface area and active site density. They found better agreement with satellite-based observations using the AF approach in combination with higher dust particle freezing efficiency as compared to the default rate-based approach, and noted an under-prediction of mixed-phase ice with the latter that led to a higher abundance of cloud droplets
360 being transported into the cirrus regime where they could undergo homogeneous nucleation. Our model median ICNC values between 230 K and 250 K indicate a similar behavior. The higher ICNC values between 230 K and 240 K, as compared to the observations, are likely of liquid-origin. Whereas, the lower ICNC values above 240 K are likely due to the under-prediction of mixed-phase ice using the default rate-based scheme for dust immersion freezing. The Villanueva et al. (2021) study suggests using a different approach for mixed-phase cloud glaciation for better comparability to observations and to address this issue
365 of an over-abundance of liquid-origin cirrus ice. Krämer et al. (2020) suggest that these liquid-origin cirrus in the mid-latitudes originate from warm conveyor belts or mesoscale convective systems. Therefore, their formation is tied to a stronger dynamical forcing that allows for abundant homogeneous nucleation from numerous cloud droplets being transported into the cirrus regime. As CCT targets in-situ formed cirrus in regions with less dynamical forcing (Gasparini et al., 2017), we deem this over-prediction of ICNC values insignificant relative to our study(Gasparini et al., 2017).

370 The model ~~does not capture the occurrence~~ diverges from the observed median at temperatures below ~~roughly 195 K~~ about 205 K. According to Krämer et al. (2020) ICNC values at such cold temperatures likely originate from tropical deep convection. Between 195 K and 205 K the model median ICNC is higher than the in-situ measurements. This may be linked to a lack of cloud-top measurements at these cold temperatures, or the fact that high ICNC values in this temperature range are short-lived and therefore difficult to capture by aircraft (Gryspeerd et al., 2018; Krämer et al., 2020). The model also does not capture
375 the ICNC occurrence at temperatures below roughly 195 K. A simple analysis on the number of data points belonging to this temperature regime shows that in the observations(~~not shown~~), there is a large drop-off in the number of recorded points (~~not shown~~). Therefore, these measurements make up a small portion of the total observational dataset. Furthermore, CCT in a real-world context would target in-situ formed cirrus away from systems with strong dynamical forcing (Gasparini et al., 2017), like in the tropics. ~~Overall,~~ The model also does not capture the wide variability of ICNC values as seen in the in-situ measurements,
380 as we compare five-year annual mean model data to instantaneous values recorded during various aircraft campaigns. However, for the purposes of our CCT analysis we find that the model ~~agrees remarkably~~ median ICNC as a function of temperature agrees well with the Krämer et al. (2020) measurements for in-situ formed cirrus.

3.2 D19 versus S89 seeding

The net global-mean radiative balance between TOA SW and TOA LW fluxes, including the net CRE is presented in Figure 3a
385 and c, respectively, for $S_{i,seed} = 1.05$. The results are tabulated along with the constituent SW and LW CRE fluxes in Table 4 ~~along~~ , with the 95 % confidence interval. ~~Small negative radiative anomalies are evident for both D19 and S89;~~ CRE fluxes are discussed below. We find no net negative mean TOA anomalies for any of our simulations except Full_S89 Seed0.1 (, but contain high uncertainty. We find the maximum amount of cooling for D19 of nearly -0.4 W m^{-2} for Table 4). Some cooling may be evident within the range of uncertainty surrounding the mean anomalies for the Seed0.1 and Seed1 (⊖) simulations

Table 4. Five-year annual global mean net top-of-atmosphere total radiative balance (TOA) and net CRE as well as SW CRE and LW CRE in Wm^{-2} for D19 and S89 ice-cloud cloud fraction approaches for seeding with $S_{i,\text{seed}} = 1.05$. Each quantity includes the 95 % confidence interval equating to two standard deviations of the mean values of the five-year data.

Seeding Concentration [L^{-1}]		Seeding Concentration				
		0.1	1	10	100	
L^{-1}	D19-net	<u>net TOA</u>	<u>$-0.17-0.18 \pm 0.32-0.12$</u>	<u>$-0.36-0.16 \pm 0.19-0.29$</u>	<u>$0.30-0.84 \pm 0.19-0.22$</u>	<u>$4.27-4.71 \pm 0.40-0.18$</u>
	S89-net	<u>net CRE</u>	<u>$-0.24-0.08 \pm 0.47-0.20$</u>	<u>$0.17 \pm 0.47-0.29$</u>	<u>$2.18-0.96 \pm 0.45-0.25$</u>	<u>$8.95-4.02 \pm 0.36-0.21$</u>
	D19-net	<u>$7.51\text{e-}4$ SW CRE</u>	<u>$0.06 \pm 0.29-0.34$</u>	<u>$-0.13-0.04 \pm 0.26-0.38$</u>	<u>$0.81-0.66 \pm 0.27-0.40$</u>	<u>$3.85-3.43 \pm 0.36-0.28$</u>
	S89-net	<u>0.13-LW CRE</u>	<u>$0.02 \pm 0.40-0.17$</u>	<u>$0.50-0.21 \pm 0.12$</u>	<u>1.61 ± 0.17</u>	<u>7.46 ± 0.19</u>
S89		<u>net TOA</u>	<u>-0.13 ± 0.39</u>	<u>0.11 ± 0.33</u>	<u>2.55 ± 0.41</u>	<u>$2.66-9.87 \pm 0.43-0.36$</u>
		<u>net CRE</u>	<u>-0.08 ± 0.28</u>	<u>0.23 ± 0.24</u>	<u>2.94 ± 0.30</u>	<u>8.51 ± 0.25</u>
		<u>SW CRE</u>	<u>-0.01 ± 0.28</u>	<u>-0.34 ± 0.25</u>	<u>-1.65 ± 0.34</u>	<u>-6.39 ± 0.31</u>
		<u>LW CRE</u>	<u>-0.07 ± 0.16</u>	<u>0.58 ± 0.16</u>	<u>4.59 ± 0.17</u>	<u>14.90 ± 0.19</u>

390 for both D19 and S89 may also produce some cooling for Seed1 due to the wide uncertainty surrounding the mean value. For
a seeding concentration of 10 L^{-1} and larger. However, as the uncertainty is high relative to the mean, a clear response at
these low seeding particle concentrations is unclear from a TOA perspective. For larger seeding concentrations ($> 10 \text{ L}^{-1}$
), the radiative anomalies indicate an overseeding response as no cooling is evident a certain warming response likely from
overseeding. Furthermore, the differences between the two cloud cover approaches become abundantly clear. The largest
395 warming occurs for Seed100, with 4.3 Wm^{-2} 4.7 Wm^{-2} (D19) and 9.0 Wm^{-2} 9.9 Wm^{-2} (S89). These responses are an
order of magnitude larger than the maximum TOA anomaly found by Gasparini and Lohmann (2016) of 0.5 Wm^{-2} at the
same seeding particle concentration and for a similar configuration of the cirrus scheme. Instead, our results more closely
resemble their simulations where seeding was applied to cirrus that could form only by homogeneous nucleation, but are more
than two times what they found at a seeding concentration of 100 L^{-1} 100 L^{-1} . This difference in results further highlights
400 the importance of a consistent approach to simulate cirrus ice microphyises microphysics (Gasparini et al., 2020), and will be
discussed further in Section 4. Section 4. In addition, the maximum responses shown here are well above the latest available
IPCC estimate at the time of writing of the effective radiative forcing from a doubling of atmospheric CO_2 from the pre-
industrial period of 3.7 Wm^{-2} (Flato et al., 2013; Myhre et al., 2017), highlighting the potential dangerous side-effects of
cirrus seeding.

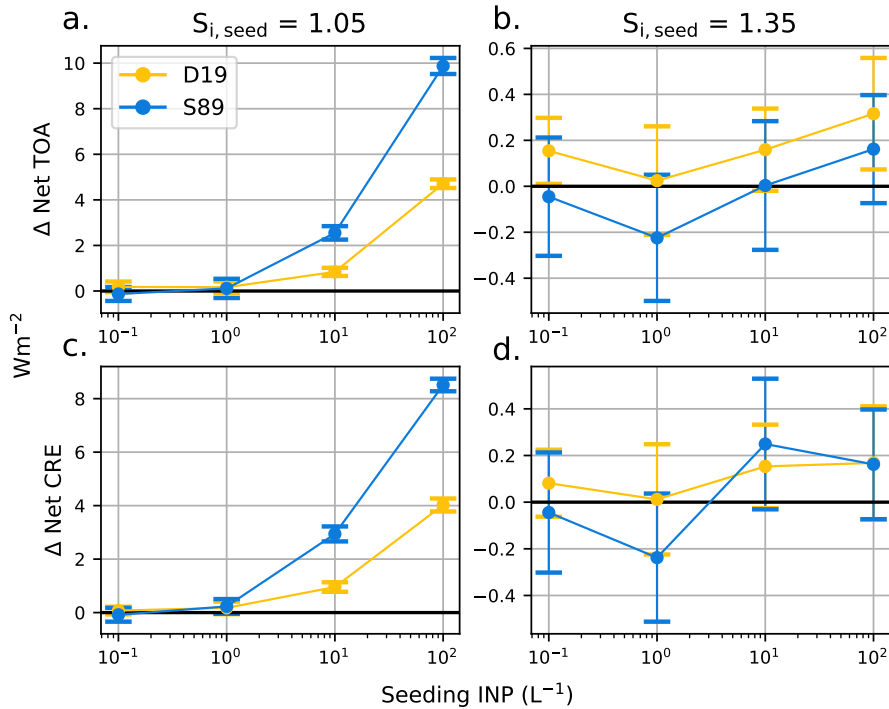


Figure 3. Five-year mean global mean net top-of-atmosphere (TOA) radiative balance anomalies in Wm^{-2} between total SW and longwave fluxes, and cloud radiative fluxes comprising the CRE. Anomalies are defined as the differences between each seeding simulation and the reference simulation without seeding. The left column (a,c) shows the radiative anomalies for simulations with $S_{i,seed} = 1.05$, and the right column (b,d) is the same for $S_{i,seed} = 1.35$. The errors bars represent the 95% confidence (2σ). Note the differences in scales for the $S_{i,seed} = 1.05$ plots and the $S_{i,seed} = 1.35$ plots.

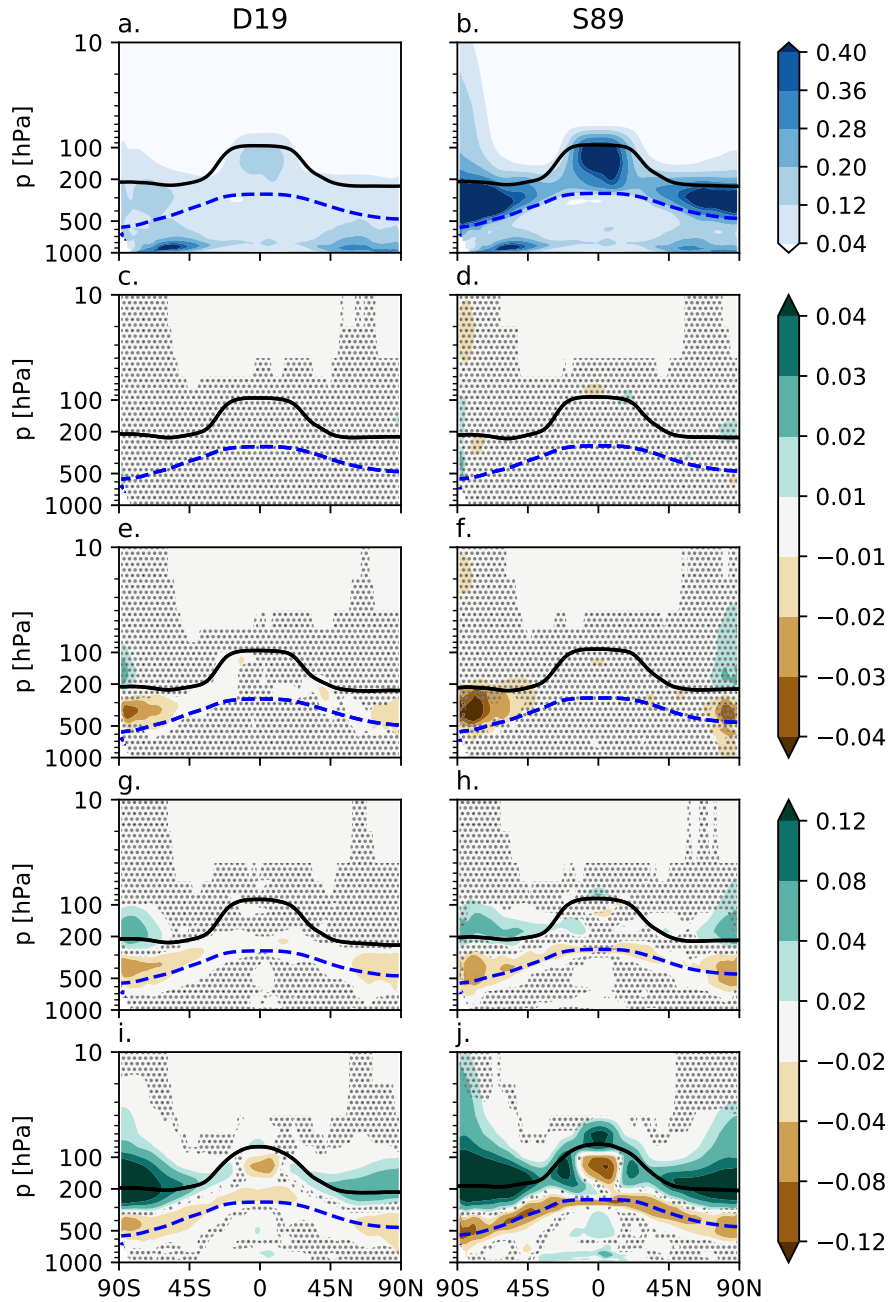


Figure 4. Five-year zonal mean cloud fractions [0-1] on pressure levels [hPa] for D19 and S89 ice-cloud fraction approaches for the unseeded reference cases ([top-panels a-b](#)). The cloud fraction [differences-anomalies](#) [respective](#) to the [respective](#) unseeded reference [case-cases](#) are plotted in the subsequent rows for $S_{i,seed} = 1.05$: Seed0.1 ([second-row c-d](#)), Seed1 ([third-row e-f](#)), Seed10 ([fourth-row g-h](#)), and Seed100 ([fifth-row i-j](#)). The black line is the five-year mean zonal mean WMO-defined tropopause height on pressure levels, and the blue dashed line is the 238 K isotherm. The stippling in the difference plots shows insignificant data points on the 95% confidence level according to the independent t-test controlled by the "false discovery rate" method.

405 Cloud effects are the largest contributor to the TOA radiative anomalies (Figure 3c and Table 4), ~~and even, in the case of Seed10, are greater than the total net anomaly, likely due to rapid adjustments in response to seeding, like cloud fraction changes.~~ In the Seed100 case, the net CRE anomalies make up ~~roughly 90%~~ around 85% of the total TOA radiative anomalies for both D19 and S89. ~~To examine this~~ Like the TOA anomalies, there is slight evidence of cooling at lower seeding particle concentrations ($< 10 \text{ L}^{-1}$) within the range of uncertainty. At higher concentrations, it is clear that clouds exert a positive
410 forcing on the atmosphere, which is fuelled by positive LW CRE anomalies (Table 4). These large anomalies are only partially counteracted by increasingly negative SW CRE anomalies at higher seeding particle concentrations, indicating perhaps a shift in cirrus formation pathway towards optically thicker liquid origin cirrus (Krämer et al., 2020) or a feedback on lower-lying liquid and mixed-phase clouds.

To examine the cloud impacts further, in particular the overseeding at high seeding particle concentrations, we show the
415 zonal mean cloud fraction anomalies between each seeding simulation and their respective reference simulation for both cloud fraction schemes in Figure 4. Firstly, the difference between D19 and S89 stands out from the respective reference simulations (top panels). With the larger S_i bounds for ice cloud fractions in D19, there is a clear cloud fraction reduction within the cirrus regime, above the blue dotted line (238 K isotherm) in Figure 4, which leads to less warming in the reference simulation compared to S89. The new cloud fractions in D19 were found to agree better with the observed satellite product from CALIPSO
420 than the original S89 approach (Dietlicher et al., 2019), ~~with higher correlation and lower root-mean-square error.~~ Secondly, a significant pattern in the zonal cloud fraction does not emerge ~~for Seed0.1. Seeding with until Seed1 appears to produce the desired reduction in cirrus cloud fractions by more than 4% that would lead to cooling. A different,~~ with small regions of cirrus cloud fraction reductions up to about 4%. S89 Seed1 shows a small region of positive cloud fraction anomaly in the stratosphere over the northern high latitudes, however the signal is not clear as all anomalies are insignificant. A clearer
425 pattern emerges for Seed10 and Seed100, where what appears as a shift in cloud height starts developing within the cirrus regime at these seeding concentrations and reaches a maximum for Seed100. Seeding decreases cloud fraction by up to 8% and 12% in D19 and S89 respectively in the mid-troposphere between 300 hPa and 800 hPa at higher latitudes, and between 300 hPa and 100 hPa in the tropics. Note that the tropopause is located at roughly 200 hPa in polar regions and at 100 hPa in the tropics, as shown by the black line in Figure 4. ~~Cloud fraction increases~~ There are noticeable cloud fraction increases around the
430 tropopause by more than 12% over ~~wider areas in the upper troposphere over the poles~~ the southern high latitudes for D19 and over all latitudes ~~in the lower stratosphere. Here the~~ for S89. The difference between the two cloud fraction approaches in this case is also clear, with S89 showing much more extensive regions of cirrus cloud fraction increases in the stratosphere than D19. The difference between the cloud fraction approaches is discussed further in ~~Section 4. In the troposphere overseeding leads to a reduction of lower-lying cirrus and the increase in higher and colder cirrus, which in turn lead to the radiative anomalies~~
435 ~~discussed above~~ Section 4. There are small regions in the lower tropical to mid-latitude troposphere (pressure $> 500 \text{ hPa}$) that show positive cloud fraction anomalies up to 4% and 8% for D19 and S89 respectively. The reduction of lower-lying cirrus and an apparent shift to more frequent higher altitude cirrus explains the large positive LW CRE anomalies in Table 4. This shift outweighs the stronger (i.e. more negative) SW CRE anomalies that likely originate from the small positive cloud

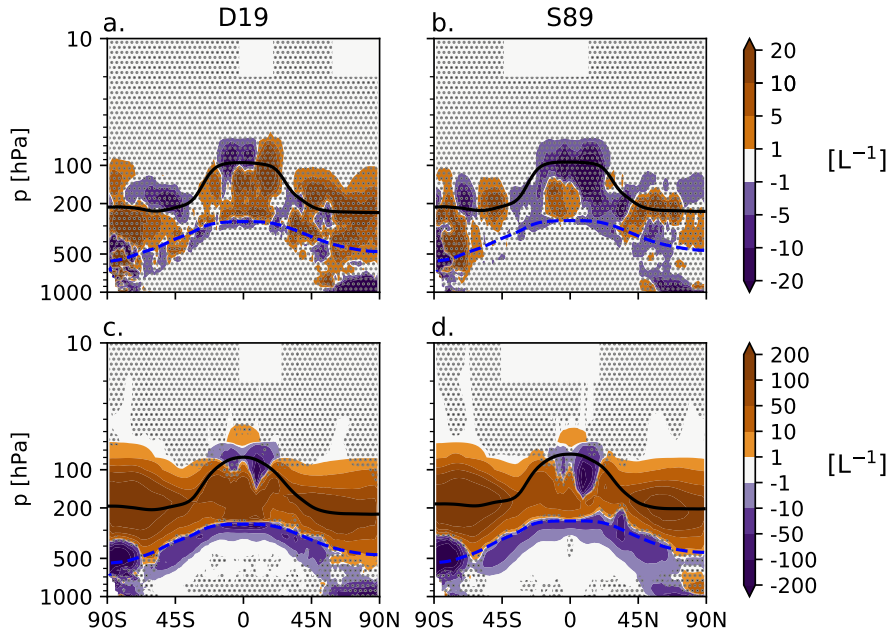


Figure 5. Five-year zonal mean ICNC $S_{i,seed} = 1.05$ anomalies in L^{-1} for both D19 and S89 ice-cloud fraction approaches. Seed1 anomalies are presented in a and b, and Seed100 anomalies are presented in c and d. The black line is the five-year mean zonal mean WMO-defined tropopause height on pressure levels, and the blue dashed line is the 238 K isotherm. The stippling in the difference plots shows insignificant data points on the 95 % confidence level according to the independent t-test controlled by the "false discovery rate" method.

fraction anomalies for lower-lying clouds. Meanwhile, the overseeding response is amplified by the unrealistic increases of
 440 cloud fraction in the stratosphere.

Next, we examine the microphysical response to seeding in Figure 5, which shows the total ICNC anomalies for Seed1 (a-b) and Seed100 (c-d) for both D19 and S89. ~~With the negative anomalies and the decrease in cloud fractions for Seed1, we expected seeding to have the desired impact of decreasing in the troposphere through sedimentation of fewer larger ice crystals. This effect is not evident here. Instead, determining~~ Determining an exact ICNC response for Seed1 is rather difficult due to
 445 ICNC anomaly heterogeneity. For ~~example, for~~ D19 Seed1 (Figure 5a), in some areas we find that seeding produces ~~fewer ice particles at higher altitudes and more at lower altitudes. This is in~~ more ice particles in widespread areas throughout the troposphere, with few areas of negative anomalies that also extend into the lower stratosphere. The opposite is the case for S89 where seeding appears to produce few ice particles particularly in the tropics, with a mixed signal towards higher latitudes. For ~~this latter case, in some regards, this is in~~ line with one of the desired outcomes of CCT to produce ice at lower altitudes, i.e.
 450 warmer temperatures, which emits more LW than higher-altitude ice, thus inducing a cooling effect. However, ~~in our case, the shift is from ice in the lower stratosphere to more ice within the cirrus regime in the troposphere. On top of this, for both our Seed1 cases,~~ our FDR analysis (Wilks, 2016) reveals that the Seed1 ICNC anomalies contain high uncertainty. ~~Despite this, the~~

cooling we find for Seed1 with D19 appears to originate from fewer clouds that on average contain more ice, which strengthens the negative Δ CRE by roughly -0.4 W m^{-2} and outweighs the positive anomaly around 0.3 W m^{-2} . The flux also increases only slightly due to fewer cirrus clouds, and contributes to the net cooling effect in (Figure 3 and Table 4) also shows high uncertainty relative to the mean response.

The ICNC anomalies are much clearer and certain for the extreme case, Seed100, than for the Seed1 anomalies (Figure 5c-d); and will be examined further in this section. Positive ICNC anomalies exceeding 200 L^{-1} are shown at all latitudes throughout the troposphere, and into the lower stratosphere at higher latitudes. The anomaly heterogeneity around the tropics is likely due to the proficiency of seeding particles to nucleate ice and hamper homogeneous nucleation in convective outflow regions around the tropopause. The ICNC anomalies at lower altitudes and towards higher latitudes are much clearer. Here the ICNC anomalies are in line with the cloud fraction anomalies in Figure 4. There is a loss of the lowermost ice crystals-ICs that also extends into the mixed-phase regime (below the blue dashed line in Figure 5), while the ICNC in the cirrus regime increases. This is most likely due to the proficiency of seeding particles to nucleate ice, leading to more numerous and smaller ice crystals-ICs that do not sediment into the mixed phase regime as readily compared to the unseeded case. In fact, we find that ICs decrease in size on average by more than $4.0 \mu\text{m}$ in the cirrus regime for Seed100 (not shown). The more abundant smaller in the cirrus regime, therefore, enhance the cirrus. In addition, with numerous seeding particles available up to 100 hPa, ICNC increases in the lower stratosphere above higher latitudes. This leads to large cloud fraction increases (Figure 4i-j) in these regions, where in the unseeded case there were fewer clouds (Figure 4a-b). Therefore, for the Seed100 case it is the combination of multiple effects that contributes to the strengthening of the LW CRE to produce by roughly 7.5 W m^{-2} and 14.9 W m^{-2} in D19 and S89 (Table 4), respectively, and the strong positive Seed100 net TOA anomaly anomalies for both cases in Figure 3.

It is clear that seeding particles in Seed10 and Seed100 lead to an overseeding effect at higher concentrations, with wide impacts on the total ICNC. However, for a direct view of the impact seeding particles have on the impact of seeding particles on ice nucleation competition, Figure 6 shows the cirrus ice number tracer (Section 2.1) anomalies for Seed100 for D19 and S89. The tracers include in-situ cirrus ice numbers from homogeneous and heterogeneous nucleation, with additional tracers for heterogeneously formed ice on mineral dust particles and seeding particles. Firstly, the anomalies presented in Figure 6 are mainly constrained to the cirrus regime, the area above the blue-dashed line, and the lower stratosphere, with some extension of anomalies into the lower-lying mixed-phase regime following ice crystal sedimentation. In terms of ice nucleation competition, Seed100 shows the desired effect by decreasing homogeneously-nucleated ice by more than 200 L^{-1} in the middle to upper troposphere in both D19 and S89. The opposite effect occurs in the stratosphere where homogeneously-nucleated ice increases. As the shift of homogeneous nucleation to lower pressure levels (Figure 6a-b), is likely due to increased LW cloud-top cooling from thicker cirrus cloud following seeding (Possner et al., 2017). This also impacts heterogeneous nucleation on mineral dust particles in the lower stratosphere. As this latter process is not sufficient at consuming water vapor, homogeneous nucleation proceeds to form additional ice crystals. This cloud top cooling effect likely also explains the heterogeneity of the total ICNC anomaly around the tropical tropopause (Figure 5). As there is a clear separation, this stratospheric effect is discussed further in Section 3.3. This between the troposphere and the stratosphere, these phenomena point to a complex impact on the stratospheric circulation, which we discuss in Section 3.4.

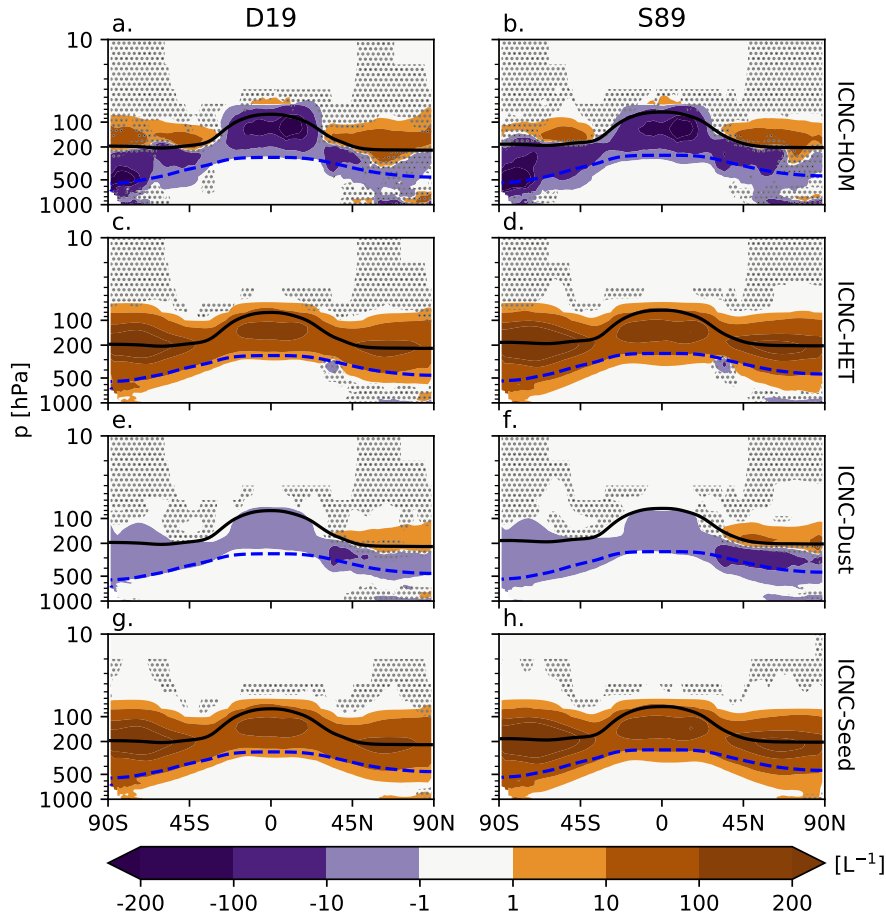


Figure 6. Five-year zonal mean in-situ cirrus ice number tracer anomalies in L^{-1} between the simulation with 100 seeding $INP L^{-1}$ for $S_{i,seed} = 1.05$ anomalies L^{-1} and the respective unseeded reference case for both D19 and S89 ice-cloud fraction approaches. Seed+ The anomalies are presented in a and b include the in-situ homogeneously-nucleated ice number (a-b), the in-situ heterogeneous number (c-d), the heterogeneously-nucleated ice number formed on mineral dust particles (e-f), and Seed100 anomalies are presented in e and d the heterogeneously-nucleated ice number formed on seeding particles (g-h). The black line is the five-year mean zonal mean WMO-defined tropopause height on pressure levels, and the blue dashed line is the 238 K isotherm temperature contour. The stippling in the difference plots shows insignificant data points on the 95% confidence level according to the independent t-test controlled by the "false discovery rate" method.

The reduction of homogeneous nucleation in the troposphere is outweighed by the wider-spread increases in heterogeneous nucleation globally throughout the middle to upper troposphere and into the lower stratosphere for both ice cloud fraction approaches, leading to the positive net TOA and CRE anomalies (Figure 3). For Seed100 the heterogeneous signal is clearly dominated by seeding particles that act to overtake dampen natural processes, including heterogeneous nucleation on dust as

490

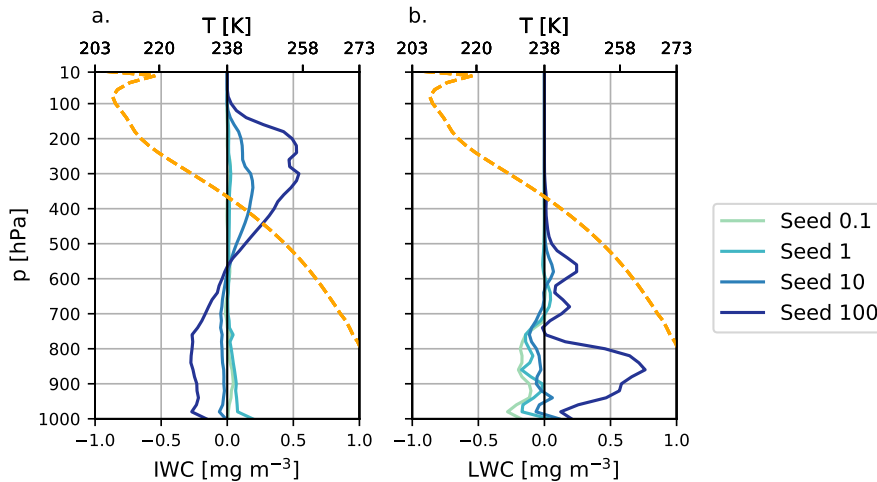


Figure 7. Five-year zonal-annual-global mean in-situ-ice-number-tracer L^{-1} anomalies between the simulation with 100 (a) IWC and (b) liquid water content (LWC) vertical anomaly profiles in mg/m^3 for D19 for all seeding L^{-1} particle concentrations for $S_{i,\text{seed}} = 1.05$ and the respective unseeded reference case for both D19 and S89 ice-cloud-fraction approaches. Each tracer is for in-situ cirrus ice only, and does not include ice formed in the mixed-phase regime. The top row is the difference for in-situ homogeneously-nucleated ice number, the second row is the difference for the in-situ heterogeneous number, the third row is the difference for the heterogeneously-nucleated ice number formed on mineral dust particles, and the last row is the difference for the heterogeneously-nucleated ice number formed on seeding particles. The black orange dotted line is represents the five-year global mean zonal-mean-WMO-defined-tropopause-height on pressure levels, and temperature vertical profile centred around the blue dashed line is the 238 K-homogeneous freezing temperature contour limit (238 K). The stippling in the difference plots shows insignificant data points on the 95% confidence level according to the independent t-test controlled by the "false discovery rate" method.

well as homogeneous nucleation. While this effect occurs in both D19 and S89, the spatial extent of the ICNC responses is more widespread in the latter in line with the smaller S_i bounds for calculating ice cloud fractions.

We also find ice crystals formed on seeding particles from the cirrus regime ending up in the mixed-phase regime (below the dashed line in Figure 6), pointing to potential impacts on lower-lying cloud layers from seeding. In fact, vertical profiles of IWC and LWC for D19 only in Figure 7 confirm this behavior. The positive Seed100 IWC anomaly within the cirrus regime right of the vertical black line in Figure 7 is in line with the total ICNC and-tracer (Figure 5) and cirrus ice tracer (Figure 6) anomalies. We also find that ice increases to a smaller extent in the upper portion of the mixed phase regime, also in line with the tracer anomalies above. The main impact of seeding appears as a reduction of IWC in wider areas of the mixed-phase regime, which and liquid regimes, the latter of which includes sedimenting ice that has not had sufficient time to melt. This is likely due to amplified ice residence times in the cirrus regime fuelled by smaller ICs that weaken the sedimentation flux. With less ice falling into the mixed-phase regime at lower altitudes, LWC anomalies responded positively (Figure 7b) due to less efficient riming and/or cloud droplet depletion via the Wegener–Bergeron–Findeisen (WBF) process. This results in a stronger

is in line with the positive, albeit small, anomalies of lower-lying cloud fractions in the tropics and mid-latitudes in Figure 4. With a higher frequency of these lower clouds, the SW CRE ~~by about 3.7 Wm^{-2} for~~ strengthens by about -3.4 Wm^{-2} for D19 Seed100 (Table 4). However, this is outweighed by the larger LW CRE positive anomaly of 7.5 Wm^{-2} due to optically thicker in-situ cirrus (Krämer et al., 2020). ~~To a smaller extent, a similar pattern is reflected in the Seed10 IWC vertical anomaly, in line with the positive LW CRE (Table 4); however, the LWC vertical anomaly is much less clear and therefore the SW CRE anomaly is much smaller with higher uncertainty relative to the mean value.~~

The patterns found in the TOA radiative anomalies, and the ICNC and IWC anomalies can be explained by the competition for water vapor during the formation of in-situ cirrus ice. The cirrus scheme is called during every time-step in the model, and the nucleation of new ~~ice crystals~~-ICs occurs only if cirrus conditions ($T < 238 \text{ K}$) are met. Seeding particles efficiently form new ~~ice crystals~~-ICs with a relatively low $S_{i,\text{seed}} = 1.05$. ~~They~~ ~~In addition, our simplified method of including seeding particles as INPs in our cirrus scheme, using a globally uniform approach (i.e. every grid box includes the same concentration of seeding particles), results in accumulation of their impacts. This resulted in ICNC anomalies that were larger than the seeding particle concentration (Figure 5 and Figure 6). As seeding particles~~ consume water vapor with increasing efficiency at higher concentrations, ~~leaving they leave~~ little supersaturated vapor left for other processes to occur, as indicated by the reduction of homogeneous nucleation and heterogeneous nucleation on mineral dust particles. This phenomenon goes beyond the traditional understanding of overseeding, where only homogeneous nucleation suppression was documented, coupled to a higher number of ICs nucleated on seeding particles (Storelvmo et al., 2013). Rather, our results show that overseeding leads to an ice nucleation competition alteration with the suppression of heterogeneous nucleation on mineral dust particles on top of homogeneous nucleation suppression. In relation to the cloud fraction responses (Figure 4), overseeding in our model appears to lead to the desired reduction of mid-troposphere clouds. However, at higher altitudes seeding particles overtake natural processes to form higher cloud fractions. As these clouds are in general colder, increases in their coverage lead to a larger TOA warming described above.

Overseeding occurs with both D19 and S89 ice cloud fraction approaches, but is more widespread with the narrower S_i bounds used in the latter. With seeding particles ~~being~~ present in every gridbox of the cirrus scheme and their relatively low $S_{i,\text{seed}}$, even small increases in ~~the amount of INPs~~ and hence the amount of ice in an ice-supersaturated environment can lead to dramatic cloud fraction increases with S89. In addition, the low $S_{i,\text{seed}} = 1.05$ "out-competes" all other freezing modes to alter nucleation competition away from natural processes and towards seeding particles with both schemes. As this critical saturation ratio threshold is somewhat arbitrary, we ~~next investigate the seeding sensitivity with needing a higher~~ ~~investigate CCT sensitivity using seeding particles with a higher critical~~ $S_{i,\text{seed}} = 1.35$ for nucleation.

3.3 1.05 S_i versus 1.35 S_i seeding

Additional sensitivity tests were conducted by increasing $S_{i,\text{seed}}$ to 1.35 (1.35-seeding) in an effort to limit the overseeding found ~~when seeding~~ with $S_{i,\text{seed}} = 1.05$ (1.05-seeding). Figure 3b presents the net TOA radiative anomaly for both cloud fraction approaches for 1.35-seeding; results are also presented along with the 95% confidence interval in Table 5. Note the difference in scale to the 1.05-seeding TOA plot (Figure 3a). ~~Not only does~~ 1.35-seeding ~~lead leads~~ to a drastic reduction ~~in~~

magnitude in of the net TOA anomalies by a whole order of magnitude for both D19 and S89, but also to a small cooling effect for all seeding concentrations, excluding the small positive with the maximum anomaly of 0.32 Wm^{-2} for D19 Seed100. We also find evidence of an optimal seeding particle concentration at 1 L^{-1} , similar to Gasparini and Lohmann (2016), as shown by the most negative anomaly for S89 Seed100, meaning that the desired cooling from seeding in our model can occur over a broader range compared to early studies (Storelvmo et al., 2013) (-0.22 Wm^{-2}) and the smallest positive anomaly for D19 (0.02 Wm^{-2}). TOA anomalies are stronger in more positive with D19 than in S89, with the strongest negative anomaly of -0.3 Wm^{-2} for Seed10. This is in part, due to a strengthening of the due to larger positive LW CRE with anomalies with increasing seeding particle concentrations for D19 (i.e. warming) that is outweighed by a stronger that exceed the small SW CRE (i.e. cooling anomalies) (Table 5). The smaller negative net TOA anomalies for S89 are driven by a weakening stronger SW CRE with seeding that is partially compensated by a weakening response in combination with a weakening of the LW CRE, except in the Seed100 case where the increase in outweighs the stronger (Table 5). However, consistent across both cloud fraction approaches is the large uncertainty relative to the absolute response, leading to uncertain responses uncertainty in the net TOA radiation and CRE in Figure 3c,d. This also applies for the net TOA response for the "optimal" concentration for Seed1. The only exception is for D19 Seed10, which on Seed100, which at the 95 % confidence level shows a net cooling effect.

With the warming effect (Table 5). With high uncertainty in both the net TOA balance and the net CRE for 1.35-seeding with both ice-cloud fraction approaches, plus the use of the unrealistic ice saturation threshold for full gridbox coverage for ice clouds in S89 (Section 3.1 Section 3.2), we focus our comparison between for the rest of this study between 1.05-seeding and 1.35-seeding with D19 only. The global mean radiative anomalies are mostly inconclusive for both 1.05-seeding and 1.35-seeding. Therefore, we examine the zonal mean anomalies for each seeding concentration for both thresholds in. The most striking finding from is that increasing to 1.35 reduces the likelihood of overseeding, and, consistent with the anomalies in, even produces cooling for all seeding particle concentrations. For Seed100 with = 1.05 (a) the maximum positive anomaly is around 13.0 Wm^{-2} in the (not shown), whereas Seed100_1.35 (b) the maximum positive radiative forcing anomaly is less than 1.0 Wm^{-2} . Remarkably, both cases show small regions of negative forcing (i.e. a cooling effect), but for lower seeding particle concentrations. Seed0.1, Seed1, and Seed10 with = 1.05 all show some degree of negative forcing around roughly 20°N , 45°N , and 70°N , whereas only Seed1 shows any appreciable negative forcing in the between 50°S and 60°S , and Seed10 centered on 30°S . 1.35-seeding shows a similar negative forcing over wider areas centered around similar latitudes, but for all seeding particle concentrations. Both scenarios show very small negative forcing in the tropics. The strongest cooling for 1.05-seeding of -1.5 Wm^{-2} occurs for Seed1 around 20°N , and for 1.35-seeding around -1.4 Wm^{-2} for Seed0.1_1.35 near the same latitude.

As Seed10_1.35 shows a small, but statistically significant cooling effect (-), plus wider areas of cooling evident in, we investigate certainty of this zonal anomaly for both scenarios with the 95 % confidence interval based on the variance of the five-year zonal data, as shown by the grey-shaded area in. The uncertainty around specific latitudes varies, with a wider 95 % confidence interval for both scenarios towards higher latitudes in the D19 only. Seed10 does appear to lead to significant cooling around the same latitudes, 40°S and 25°N for both scenarios, but the cooling is more evident and

Table 5. Five-year annual global mean net top-of-atmosphere total radiative balance (TOA) ~~in the Northern and Southern Hemispheres~~ between 60°N/S net CRE, as well as SW CRE and 90°N/S LW CRE in Wm^{-2} for D19 and S89 ice-cloud fraction approaches for seeding ~~with a critical ice saturation ratio of 1.05 and at $S_{i,seed} = 1.35$.~~ Each quantity includes the 95 % confidence interval equating to two standard deviations of the mean values of the five-year data.

Seeding Concentration [L^{-1}]		Hemisphere-			
		<u>$S_{i,seed} 0.1$</u>	<u>Seed0.1</u>	<u>Seed1</u>	<u>Seed10</u> <u>Seed100</u> <u>100</u>
Northern- Southern- D19	<u>net TOA</u>	<u>-0.13-0.15 ± 1.12-0.24</u>	<u>-0.04-0.02 ± 1.28-0.29</u>	<u>0.16 ± 0.94-0.19</u>	<u>3.63-0.32 ± 1.73-0.19</u>
	<u>net CRE</u>	<u>-0.04-0.08 ± 0.67-0.15</u>	<u>-0.09-0.01 ± 0.82-0.25</u>	<u>2.13-0.15 ± 0.76-0.20</u>	<u>9.85-0.17 ± 1.73-0.26</u>
	<u>SW CRE</u>	<u>-0.01 ± 0.24</u>	<u>-0.01 ± 0.24</u>	<u>0.03 ± 0.36</u>	<u>0.02 ± 0.34</u>
	<u>LW CRE</u>	<u>0.10 ± 0.14</u>	<u>0.02 ± 0.13</u>	<u>0.12 ± 0.20</u>	<u>0.15 ± 0.15</u>
Northern- Southern- S89	<u>net TOA</u>	<u>-0.15-0.05 ± 0.89-0.31</u>	<u>-0.62-0.22 ± 1.17-0.42</u>	<u>-0.31-0.00 ± 1.06-0.31</u>	<u>-0.25-0.16 ± 0.72-0.37</u>
	<u>net CRE</u>	<u>-0.41-0.04 ± 0.60-0.28</u>	<u>-0.18-0.24 ± 0.71-0.29</u>	<u>0.25 ± 0.28</u>	<u>0.16 ± 0.26</u>
	<u>SW CRE</u>	<u>-0.01 ± 0.28</u>	<u>-0.16 ± 0.50-0.30</u>	<u>0.22-0.24 ± 0.51-0.33</u>	<u>0.01 ± 0.28</u>
	<u>LW CRE</u>	<u>-0.03 ± 0.16</u>	<u>-0.07 ± 0.19</u>	<u>0.01 ± 0.18</u>	<u>0.15 ± 0.18</u>

575 statistically significant with 1.35-seeding. The minimal cooling towards higher latitude regions contrasts previous findings (Storelvmo and Herger, 2014; Storelvmo et al., 2014). However, to examine these higher-latitude regions further, presents the five-year mean net anomalies between 60°N/S and 90°N/S as well as the 95 % confidence interval around the mean. For 1.05-seeding, the strongest cooling occurs for Seed0.1 in the and for Seed1 in the . As shown previously, cooling occurs for all seeding particle concentrations for 1.35-seeding, except for Seed100_1.35 in the , with the strongest cooling for Seed1_1.35 in the . However, the uncertainty for seeding particle concentrations for both scenarios is much higher than the mean anomalies. Therefore, our results in this case only partially support the idea of an optimal seeding particle concentration around $1 L^{-1}$ (Gasparini and Lohmann, 2016). Furthermore, our results cannot confirm the findings that higher latitude regions are the most desirable for implementation (Storelvmo and Herger, 2014; Storelvmo et al., 2014; Gruber et al., 2019), as the net zonal anomalies are rather uncertain.

585 ~~We compare the~~ As the Seed1_1.35 scenario showed the smallest positive TOA anomaly, with cooling possible within the range of uncertainty, we examine the microphysical response by comparing the zonal mean in-situ ice tracer anomalies for Seed10 and Seed10Seed1 and Seed1_1.35 in Figure 8 ~~as this case showed statistically significant cooling for 1.35-seeding.~~ Homogeneously-nucleated. There is no clear response in the homogeneously-nucleated ice number anomalies within the cirrus regime (above the 238 K isotherm, dashed line in Figure 8) ~~in for~~ both 1.05-seeding and 1.35-seeding ~~eases appear to overlap to some extent with the latitude bands that showed negative forcing anomalies in . Seeding in these regions appears to lead to the desired shutting off of homogeneous nucleation. Plus, the overall zonal mean anomalies for both cases are uncertain according~~ the our FDR analysis. The signal is clearer in the in-situ heterogeneous tracer anomaly where positive values are much more ~~wide spread~~ widespread and certain for 1.05-seeding than 1.35-seeding. Heterogeneous nucleation increases by more than

10 L⁻¹ in most regions for 1.05-seeding, and to a lesser extent with 1.35-seeding. ~~The latter shows higher uncertainty in the response, which points~~ There is less certainty in the 1.05-seeding case towards higher latitudes in the northern hemisphere (NH) where it also shows large positive anomalies, whereas the 1.35-seeding case shows negative anomalies. The differences in the responses between 1.05-seeding and 1.35-seeding point to the difference in ice nucleation competition between the two cases. With the former, we find a similar situation as before, where heterogeneous nucleation on dust is overtaken by heterogeneous nucleation on seeding particles. For ~~Seed10-Seed1~~ this switch to seeding-particle-dominant heterogeneous nucleation within cirrus clouds ~~appears to lead to~~ leads to a small positive TOA effect (Figure 3 and Table 4). We find ~~the opposite a much smaller~~ TOA response with ~~Seed10Seed1~~ 1.35. Seeding particles in this case appear to shut off heterogeneous nucleation on mineral dust ~~between roughly 45°N/S~~ only in small regions between roughly 45°N and 90°N, and to a lesser extent in the southern hemisphere (SH) up to around 60°S. On the other hand, the amount of dust-driven nucleation increases towards higher latitudes in the SH and in the Tropics. However, both homogeneous and heterogeneous nucleation ice tracers for 1.35-seeding contain high uncertainty as shown by the stippling in Figure 8. The seeding ice tracer anomaly is more certain and shows increases of ~~more than 10 L⁻¹~~ up to 1 L⁻¹ in the tropics, ~~but and~~ is much less widespread than the 1.05-seeding scenario. This is due to the fact that a S_i of 1.35 occurs much less often in the atmosphere than a S_i of 1.05. Therefore, seeding particles with a higher S_{i,seed} are much less efficient in this case at consuming water vapor to overtake other nucleation modes like in the 1.05-seeding scenario, leading to the insignificant zonal ice tracer anomalies, despite a clear significant positive anomaly of heterogeneous nucleation on seeding particles (Figure 8h).

~~The uncertainty in the~~ The global mean TOA radiative anomalies as well as the zonal mean ICNC tracer anomalies ~~for are~~ mostly inconclusive for both 1.05-seeding and 1.35-seeding ~~makes it difficult to understand the physical responses to a higher~~. Therefore, we examine the zonal mean TOA anomalies for each seeding concentration for both S_{i,seed} ~~despite some evidence of a regional sensitivity to seeding particles thresholds in~~ Figure 9. The most striking finding from Figure 9 is that increasing S_{i,seed} to 1.35 reduces the likelihood of overseeding, producing more regions of cooling for all seeding particle concentrations. For Seed100 with S_{i,seed} = 1.05 (Figure 9a) the maximum positive TOA anomaly is around 13.4 Wm⁻² in the SH (not shown), whereas Seed100 1.35 (Figure 9b) the maximum positive radiative forcing anomaly is about 1.2 Wm⁻². Remarkably, both S_{i,seed} cases show small regions of negative forcing (i.e. a cooling effect), but for lower seeding particle concentrations. For the 1.05-seeding case Seed0.1 and Seed1 show some degree of negative forcing around roughly 50°S, 15°S, and centered around 30°N. The cooling for Seed0.1 around 50°S is the only appreciable signal at roughly -1.2 Wm⁻². Seed10 shows only a small degree of cooling at 30°S, with a small region with a maximal cooling of -0.7 Wm⁻² between 75°N and 90°N. As the Seed1 global mean anomaly indicated an optimal seeding particle concentration in Figure 3, we plotted the 95 % confidence interval around the mean zonal profile, which shows high uncertainty for 1.05-seeding. ~~In addition, previous studies suggested that~~ 1.35-seeding shows negative forcings in similar latitude regions, but for all seeding particle concentrations (Figure 9b). The 95 % confidence interval is plotted around the Seed1 zonal mean anomaly here as well. For the Seed1 anomaly, two regions around 45°S and between 70°N and 90°N show the largest amount of cooling. There is minimal cooling for Seed1 towards lower latitudes. The largest negative anomaly is -1.5 Wm⁻² in the northern polar region, perhaps indicating a higher CCT ~~contains seasonal sensitivity (Storelvmo and Herger, 2014; Storelvmo et al., 2014) that we have not captured in our annual~~

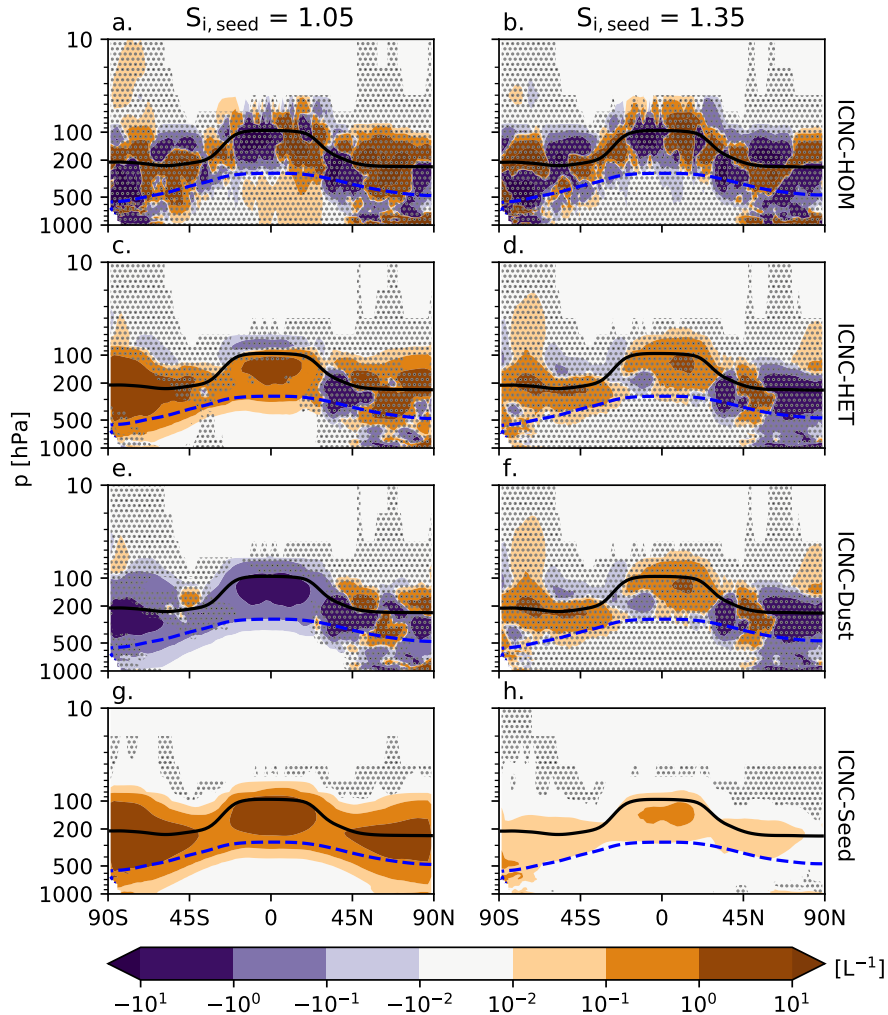


Figure 8. Five-year zonal mean ice number tracer anomalies in L^{-1} differences between the Seed10-Seed1 simulation and the unseeded reference case D19 for seeding particle critical saturation ratios 1.05 (left) and 1.35 (right). The top row is anomalies include the difference for in-situ homogeneously-nucleated ice number (a-b), the second row is the difference for the in-situ heterogeneous number (c-d), the third row is the difference for the heterogeneously-nucleated ice number formed on mineral dust particles (e-f), and the last row is the difference for the heterogeneously-nucleated ice number formed on seeding particles (g-h). The black line is the five-year mean zonal mean WMO-defined tropopause height on pressure levels, and the blue dashed line is the 238 K temperature contour. The stippling in the difference plots shows insignificant data points on the 95 % confidence level according to the independent t-test controlled by the "false discovery rate" method.

mean analysis to this point, which may be dampening a signal in our results. To address this, we examine seasonal differences in zonally-averaged efficacy towards higher latitudes as well in our model (Storelvmo and Herger, 2014; Storelvmo et al., 2014).

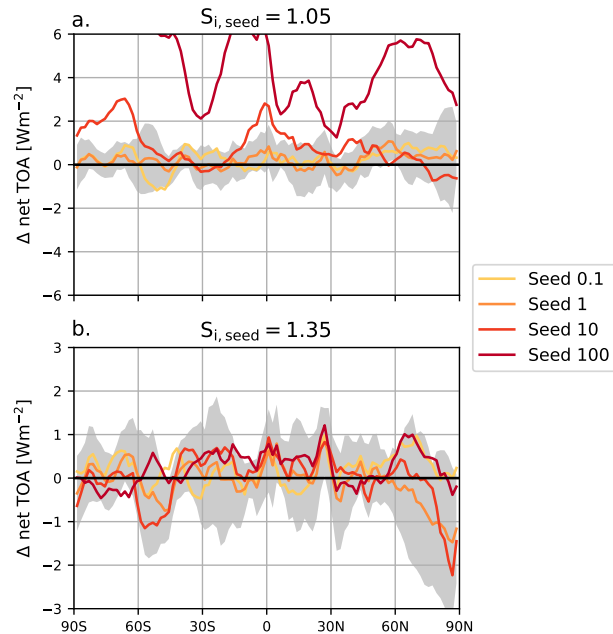


Figure 9. Five-year zonal mean net top-of-atmosphere (TOA) radiative balance anomalies in Wm^{-2} between total SW and LW fluxes for a critical seeding particle saturation ratio of (a) 1.05 and (b) 1.35 for each seeding particle concentration minus the reference unseeded D19 simulation. The grey shaded area is the 95% confidence interval, representing the two-times standard deviation interval, of the Seed1 anomaly based on the variance of the five-year data.

630 However, like the 1.05-seeding case, the uncertainty around the Seed1 zonal mean anomaly is high. Therefore, it is difficult to determine the exact radiative response around the two regions with the largest amount of cooling.

The indication that high latitude seeding may lead to a strong negative response in the Seed1 1.35 zonal anomaly in Figure 9 is in line with previous findings by Storelvmo and Herger (2014) and Storelvmo et al. (2014). To examine these higher-latitude regions further, Table 6 presents the five-year mean net TOA radiative flux anomalies in for anomalies between 60°N/S and 90°N/S as well as the 95% confidence interval around the mean. For 1.05-seeding, the only cooling response occurs for Seed10 in the four seeding particle concentrations-NH, but contains an uncertainty one order of magnitude higher than the mean.

640 There is a clear overseeding response in both hemispheres for Seed100, with mean responses exceeding the net TOA anomaly (Table 4). As shown previously, the positive anomalies are drastically reduced for 1.35-seeding. The net, which shows negative anomalies for Seed1 and Seed10 in the NH, and Seed10 and Seed100 in the SH. The largest cooling response of about -0.8 Wm^{-2} occurs for the Seed1 anomaly in the NH, but consistent with the other responses is highly uncertain.

Our results in this case only partially support the idea of an optimal seeding particle concentration around 1 INP L^{-1} (Gasparini and Lohmann, 2016). Furthermore, based on the uncertainty our annual mean results cannot confirm the findings

Table 6. Five-year annual mean net top-of-atmosphere total radiative balance in Wm^{-2} in the Northern and Southern Hemispheres between 60°N/S and 90°N/S for D19 for seeding with a critical ice saturation ratio of 1.05 and 1.35. Each quantity includes the 95 % confidence interval equating to two standard deviations of the mean values of the five-year data.

Hemisphere	$S_{i,seed}$	Seed0.1	Seed1	Seed10	Seed100
Northern	1.05	0.69 ± 0.87	0.41 ± 1.10	-0.13 ± 1.20	4.83 ± 1.34
Southern		0.35 ± 0.45	0.19 ± 0.60	2.20 ± 0.53	10.59 ± 0.74
Northern	1.35	0.44 ± 1.35	-0.77 ± 1.37	-0.51 ± 1.22	0.44 ± 1.07
Southern		0.33 ± 0.76	0.16 ± 0.64	-0.07 ± 0.49	-0.23 ± 0.33

from previous studies that higher latitude regions are the most desirable for CCT implementation (Storelvmo and Herger, 2014; Storelvmo et al., 2014). Therefore, we examine whether there is a seasonal sensitivity on CCT efficacy. Figure 10 that shows the NH winter and summer zonal mean TOA (i.e., the balance between radiative anomalies as well as the constituent SW and LW) flux anomalies for 1.35-seeding. The net TOA is presented in the first column for NH winter (top) and summer (bottom), with the SW and LW flux anomalies in the second and third columns respectively. Uncertainty is plotted around the Seed10Seed1_1.35 mean anomaly. A clear seasonal pattern is difficult to decipher from the TOA anomalies, except that in the there appear to be more widespread TOA anomalies during NH seeding appears to lead to the desired cooling only during summer/winter. In the northern polar regions (north of 60°N), only the Seed1 TOA anomaly shows a cooling response during NH winter around -3.0Wm^{-2} , in line with the findings in Figure 9 and Table 6 above. Due to the negligible SW flux at high latitudes during winter, the net TOA response is entirely driven by LW anomalies. Our model suggests that seeding particles act to enhance the already in this case act to reduce the large LW CRE in this region (roughly 10.0Wm^{-2} around 75°N 11.0Wm^{-2} in the unseeded case) to produce only positive/negative TOA anomalies. However, the uncertainty is high in the The uncertainty around the Seed1 mean anomaly in this region is high (Figure 10- During-); however, we find that cooling north of about 70°N is within the 95 % confidence interval. We also find smaller regions of cooling with net negative TOA responses for Seed1 during NH summer it appears that seeding particles act to enhance the -, as noted by the negative winter in the SH (summer) around 45°S , and between the Equator and 30°S (Figure 10a). The net TOA response is driven mainly by negative SW anomalies in -, which outweighs the small positive -, indicating either a shift in cirrus formation pathway or an impact on lower-lying mixed phase clouds.

During NH summer the net TOA response is smaller overall than during NH winter. For the Seed1_1.35 zonal mean anomaly we find only small regions of cooling in the NH and in the SH polar regions. However, the uncertainty is wide enough in this case that we cannot determine the exact radiative impact in these regions. The small cooling shown towards high latitudes in the SH is driven by LW anomalies. In fact, we find that the emission due to a lack of SW in the unseeded reference case greatly exceeds the radiation during SH winter, but like the net TOA anomaly it is highly uncertain. The few regions of cooling we find in the NH are driven primarily by SW anomalies, highlighting a potential feedback on cirrus cloud formation

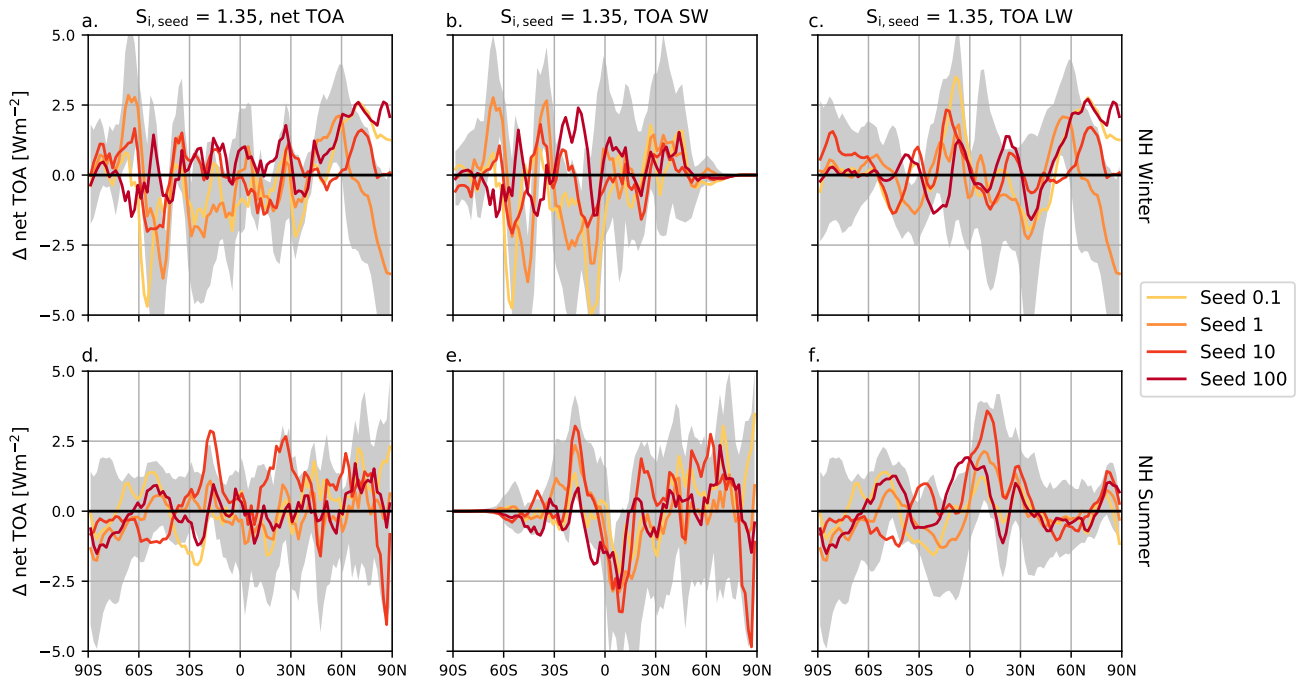


Figure 10. 1.35-seeding zonal mean radiative balance anomalies in Wm^{-2} for all seeding particle concentrations for the net TOA (a,d), the TOA SW (b,e), and TOA LW (c,f). The top row shows the four-year zonal mean for NH winter (December - February) and the bottom row is the five-year zonal mean for NH summer (June - August). The grey shaded area is the 95 % confidence interval around the mean Seed1 anomaly, representing the two-times standard deviation interval, based on the variance of the annual data.

or on mixed-phase clouds, but these are compensated by positive LW between 60°N and 90°N during this period anomalies. This is especially noticeable in the northern hemisphere tropics around the location of the Intertropical Convergence Zone (ITCZ). Thicker in-situ cirrus clouds in this case may contain some to some extent reflect more SW compensation as a result of seeding (Krämer et al., 2020), similar to the Twomey effect for lower-lying liquid or mixed-phase clouds (MPCs). This is somewhat in line with findings by Krämer et al. (2020), however we do not find evidence of a cirrus altitude shift to lower levels that could reduce their warming effect. However, they also induce a strong compensating LW effect as a result of seeding.
A more likely explanation is that 1.35-seeding impacts lower-lying mixed-phase clouds.

Figure 11 shows the vertical profiles of IWC and LWC anomalies for each seeding particle concentration, like in Figure 7 but for 1.35-seeding. Unexpectedly, we find that 1.35-seeding does not impact IWC within the cirrus regime, and leads to only very small positive anomalies in the mixed-phase regime. Instead and liquid regimes. There does appear to be a feedback on lower-lying clouds as the LWC for the anomalies are larger. LWC increases in the middle of the mixed-phase regime by a small amount only for Seed10_1.35 ease increases and Seed100_1.35, whereas in the lowermost part of the mixed-phase regime by around 0.5 mg m^{-3} , and even more so LWC decreases for all seeding particle concentrations. Seed1_1.35 shows a larger

Figure 11. Five-year annual global mean (a) IWC and (b) ~~liquid-water-content~~LWC anomaly profiles in mg/m^3 as in Figure 7, but for $S_{i,\text{seed}} = 1.35$.

680 positive LWC anomaly in the liquid phase regime. The lack of an IWC response, combined with the increase in heterogeneously nucleated ice on seeding particles and to some extent on mineral dust for Seed10Seed1_1.35, indicates that seeding impacts the size of ~~ice crystals~~ICs, which in turn affects sedimentation from the cirrus regime. Ice crystal size anomalies are also highly uncertain for the 1.35-seeding case (not shown), ~~but indicate smaller ice crystals by about $1.0\ \mu\text{m}$ throughout with up to $2.0\ \mu\text{m}$ smaller~~ ICs in the cirrus regime. It is therefore likely that seeding particles in this case partially compensate the loss

685 of ice formed on mineral dust in ~~the tropics, and some regions, while they~~ contribute to more numerous ~~ice crystals in the extra-tropics~~ ICs in others (Figure 8) to form smaller ~~ice crystals~~ ICs that weaken the sedimentation flux into the mixed-phase regime. The lack of large ~~ice crystals~~ ICs in the mixed-phase regime ~~reduces cloud droplet consumption via the WBF process or riming, and increases LWC~~ Lower-lying clouds with a higher at least for two of our scenarios. In these cases, the positive LWC likely contribute to the strengthening of the

690 ~~We also find summer cooling as a result of seeding in the (a). Seed10_1.35 also produces a net cooling effect of more than $-2.5\ \text{Wm}^{-2}$ around 60°S that is driven mostly by a weaker flux. This behavior is in direct contrast with previous findings by Storelvmo and Herger (2014); Storelvmo et al. (2014) who found that high latitude regions during winter were more susceptible to seeding to produce strong cooling effects. The lack of a cooling response in our model during winter highlights the high annual variability of cirrus cloud properties~~ anomalies in the upper mixed-phase regime may equate to

695 smaller cloud droplets that lead to a weaker sedimentation flux, which may ~~be driven by large fluctuations of annual mean dust concentrations from the larger dust sources in the~~ be driven by large fluctuations of annual mean dust concentrations from the larger dust sources in the. The only appreciable wintertime cooling we find is in the (bottom row of)where seeding produces cooling in a small region around 80°S driven by an enhanced flux. We reiterate here, however, that the seasonal, zonal-mean flux anomalies are surrounded by wide 95% confidence intervals at high latitudes, therefore making the response uncertain. result in few cloud droplets in the lowermost part of the mixed-phase regime. The small positive LWC

700 anomalies in lower-lying liquid clouds likely contribute to the slightly more negative SW CRE (Table 5), but the uncertainty is high.

3.4 Stratospheric Effects

So far our analysis focused on the changes in the troposphere leading to the TOA overseeding presented in Figure 3. However, our findings also point to stratospheric effects as a results of seeding, particularly the positive ICNC anomalies in the lower

705 stratosphere (Figure 5) and the subsequent cloud fraction increase (Figure 4). The former can be partially explained by the seeding strategy we utilize in our cirrus scheme. Seeding particles are available in every gridbox of the cirrus scheme up to the 100 hPa pressure level. This places some of our seeding particles firmly within the troposphere in the tropics, but in the lower stratosphere in the mid and high latitudes. Therefore, seeding particles are present in environments with little competition between mineral dust (i.e. low INP environments) or liquid sulphate particles, leading to wide extents of the lower stratosphere

710 with large positive ICNC anomalies. Cloud fraction increases accordingly with larger ice crystal number concentrations from seeding. This effect is more widespread with S89 than D19 due to the ice saturation threshold for full gridbox coverage of ice clouds used in the former.

What remains unclear is the positive in-situ homogeneously-nucleated ice number anomaly in the mid-latitudes and towards the poles in the lower stratosphere (Figure 6, top panel), and the higher cloud fractions that extend to pressure levels less than 100 hPa (i.e. at higher altitudes). As both cloud fraction approaches are relative humidity based, the patterns observed in
715 stratospheric cloud fraction indicate a dynamic response to the INP perturbations by increasing temperature and consequently enhancing upwelling of water vapor into the stratosphere from the tropical troposphere as shown in Figure 12. The anomalies for lower seeding concentrations and for all simulations with $a_{S_{i,seed}} \approx 1.35$ are insignificant according to the FDR method. Here, we only present the anomalies at pressure levels lower than 300 hPa (higher altitudes) to focus on the effects in the upper
720 troposphere and the stratosphere.

Overseeding in Seed100 leads to a positive temperature anomaly of more than 4 K in the tropical troposphere (Figure 12a). As a result of warmer temperatures, the saturation specific humidity increases. Therefore, the specific humidity can increase as well (Figure 12b). This appears to enhance water vapor upwelling into the lower stratosphere from the tropical troposphere, as indicated by the positive specific humidity anomaly above the tropopause (Figure 12b) that also extends into the middle
725 stratosphere. Water vapor in the stratosphere has a cooling effect (Rind and Lonergan, 1995), as indicated by the temperature response above the tropopause in the tropics and between 45 °N/S and 90 °N/S. In the same region, updraft velocities increase by more than 0.2 cm s^{-1} . As we observe larger ice-cloud fractions in this region (Figure 4), enhanced LW cloud-top cooling likely fuels the observed positive updraft anomaly. We find LW-cooling in the tropics in upper troposphere and in the extra-tropics in the stratosphere in Figure 13. The latter is likely due to the positive water vapor anomaly in the lower stratosphere
730 (Figure 12b). At lower levels we find LW warming, likely caused by more trapping from more frequent and optically thicker cirrus clouds. The increase in updraft velocity, in combination with the positive specific humidity anomaly, not only allows the seeding particles to form abundant ice particles, but also allows air parcels to reach the critical saturation for homogeneous nucleation. There are also small areas in the lower stratosphere where the anomaly of ice formed heterogeneously on mineral dust particles is positive (Figure 6). This enhancement of natural ice formation processes at lower levels in the stratosphere in
735 response to overseeding in the troposphere ([Section 3.1](#)[Section 3.2](#)), plus the widespread positive anomaly of ice formed on seeding particles in the same region leads to a higher abundance of clouds that likely contribute to the overall TOA warming effect (Figure 3).

The temperature anomaly presented in Figure 12a is not restricted to the lower stratosphere where we find enhanced ice formation, which indicates that seeding could impact the wider stratosphere as a whole via a dynamic feedback on the Brewer-
740 Dobson Circulation (BDC), (Butchart and Scaife, 2001; Rind et al., 2001; Butchart et al., 2006; Butchart, 2014). The BDC describes the global mass transport from the troposphere into the stratosphere, where air rises in the tropics and descends over higher latitudes. One of the main findings following numerous studies on greenhouse-gas driven climate change is a speeding up of this overturning circulation, with enhanced tropical mass upwelling, leading, in general, to a cooler stratosphere and a warmer troposphere (Butchart, 2014). Calvo et al. (2010) studied the enhancement of gravity wave-fueled tropical upwelling

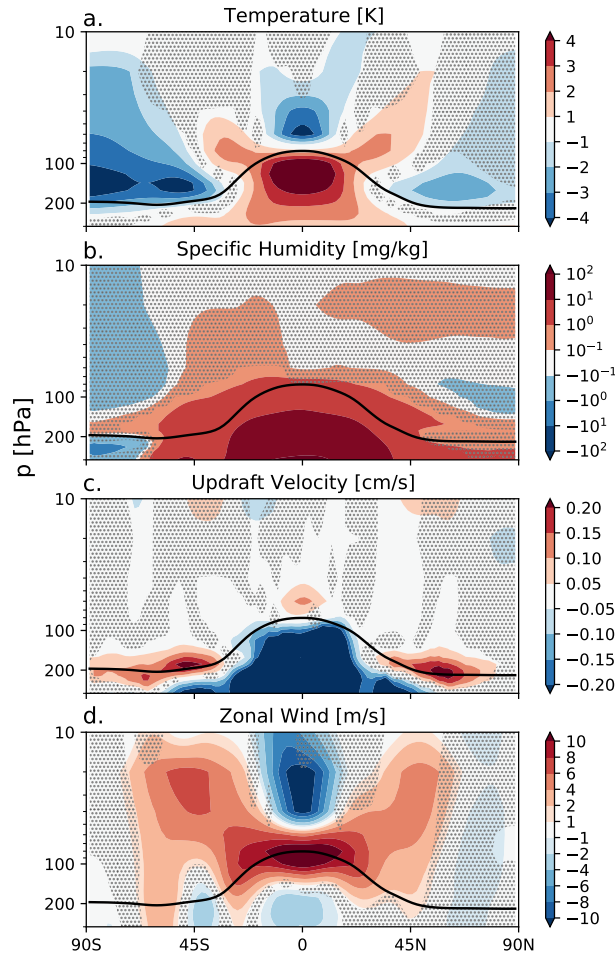


Figure 12. Five-year zonal mean [anomalies of](#) (a) temperature [in K](#), (b) specific humidity [in mg/kg](#), (c) updraft velocity [in cm/s](#), and (d) zonal wind [anomalies in m/s](#) for D19 with a seeding particle concentration of 100 INP L^{-1} . Anomalies are only shown for the upper troposphere and the stratosphere between 300 hPa and 10 hPa. The black line is the five-year mean zonal mean WMO-defined tropopause height on pressure levels. The stippling in the difference plots shows insignificant data points on the 95 % confidence level according to the independent t-test controlled by the "false discovery rate" method.

745 into the stratosphere during warm El Niño-Southern Oscillation (ENSO) events. They found that during such events tropo-
 spheric warming paired with tropical stratospheric cooling enhances the meridional temperature gradient. This strengthens the
 subtropical-jet, as seen by the increase in the zonal mean zonal wind, which is proportional to enhanced gravity wave drag
 forcing that fuels increased tropical upwelling (Calvo et al., 2010). Our results show a similar response with the positive tem-
 perature anomaly in the tropical tropopause (Figure 12a) that subsequently intensifies the sub-tropical jet, which we diagnosed
 750 from the zonal mean zonal wind anomaly in Figure 12d. The updraft anomaly in Figure 12c on the one hand shows a negative

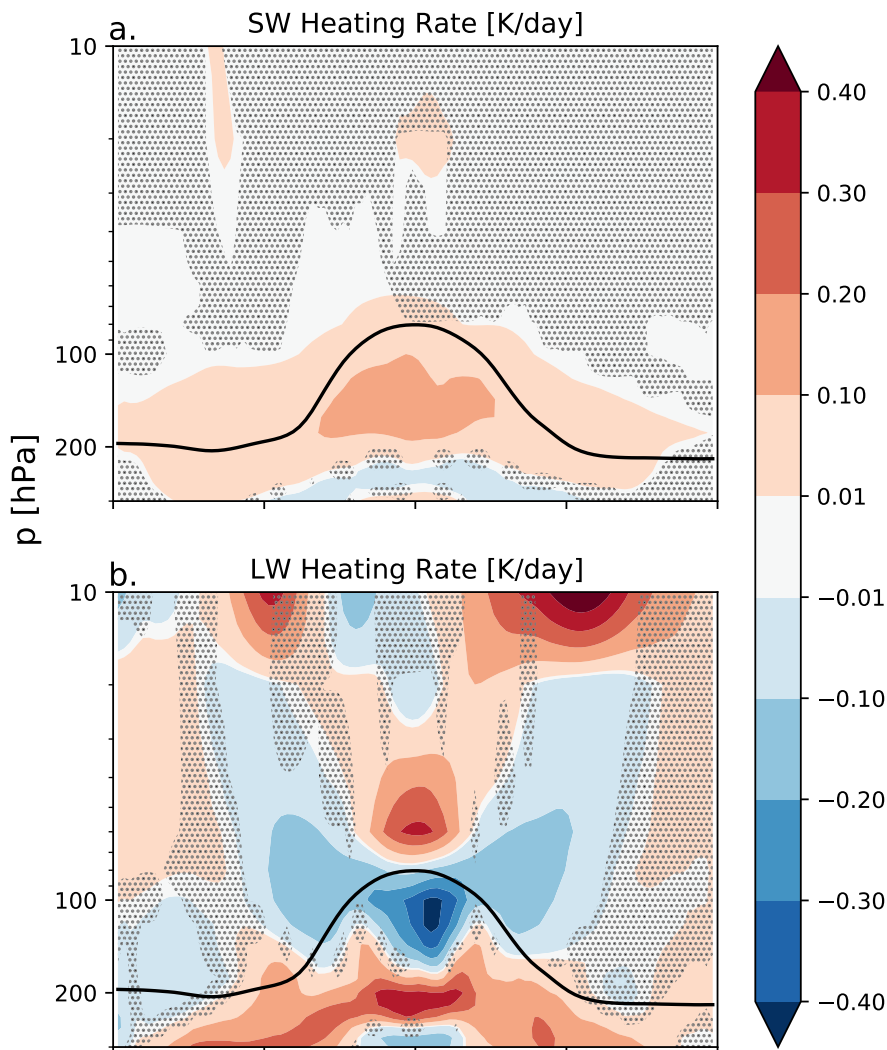


Figure 13. Five-year zonal mean (a) SW, and (b) LW heating rate anomalies [in K/day](#) for D19 with a seeding particle concentration of 100 INP L^{-1} . Anomalies are only shown for the upper troposphere and the stratosphere between 300 hPa and 10 hPa. The black line is the five-year mean zonal mean WMO-defined tropopause height on pressure levels. The stippling in the difference plots shows insignificant data points on the 95 % confidence level according to the independent t-test controlled by the "false discovery rate" method.

updraft anomaly in the troposphere as a result of enhanced atmospheric stability due to a warmer upper troposphere, similar to the stabilization found by Kuebbeler et al. (2012) following stratospheric sulphur injections. On the other hand the positive updraft anomaly indicates a small enhancement of tropical upwelling in the stratosphere that would indicate a strengthening of the BDC. However, with this effect, the downward branch of the BDC leads to stronger warming in the stratosphere at higher latitudes (see Figure 6 from Calvo et al. (2010)) due to adiabatic compression. Our results show a negative temperature anomaly

755

at high latitudes in contrast to BDC-enhancement findings, rather pointing to a weakening of the downward branch. Instead, our results point to enhanced radiative cooling of the lower stratosphere in response to positive specific humidity anomalies.

4 Discussion

The results we presented in this study highlight a few important factors governing the sensitivity of CCT, namely, the approach for calculating ice-cloud fractions, the representation of [cirrus ice nucleation competition and](#) stratiform ice microphysics, and the choice of $S_{i,seed}$ for ice nucleation to occur on seeding particles. Our results also show the potential for unwanted side-effects of CCT on mixed-phase clouds and in the stratosphere.

In a first step, we tested the sensitivity of CCT between the original approach in ECHAM-HAM for calculating cloud fractions by Sundqvist et al. (1989), (S89) and the updated approach by Dietlicher et al. (2018, 2019), (D19). Overall we found that the D19 scheme reduces net TOA warming (i.e. the positive radiative forcing) by a factor of more than two for Seed100 compared to S89 (Figure 3). Similar to the findings by Gasparini and Lohmann (2016), more frequent ice formation on seeding particles in our simulations led to cirrus cloud formation in previously cloud-free regions, using both ice-cloud fraction approaches, ~~that was especially evident with the low of 1.05~~. The conceptual difference between the two cloud fraction approaches can explain why positive cloud fraction anomalies were not as large with D19 than S89. With ~~S89~~ [the latter](#), the ice saturation threshold for full gridbox coverage of cirrus clouds meant that more frequent ice formation on seeding particles in ice supersaturated conditions artificially expanded cloud fractions to unity, increasing the zonal average cloud fraction by more than 12%. On the other hand, while the reduction of homogeneous nucleation with D19 (Figure 6) reduced the frequency of fully covered grid boxes, the increase of heterogeneous nucleation on seeding particles increased the fractional cloud cover. Therefore, while both approaches showed a positive radiative effect as a result of seeding, D19 responses are lower because ice formation at a supersaturation suitable for heterogeneous nucleation on seeding particles does not induce as high cloud fractions as in S89. This highlights limitations in both approaches for calculating ice cloud fractions. Where S89 artificially expanded ice-cloud fractions upon ice formation at supersaturation with respect to ice, ice-cloud fractions using D19 might be artificially low following seeding due to the criterion for full gridbox ice-cloud coverage only reached at homogeneous nucleation conditions. These limitations have wider implications on the radiative transfer calculations used to ~~calculate~~ [compute](#) TOA fluxes. The prognostic cloud scheme by Muench and Lohmann (2020) that explicitly calculates variables for cloud-free and cloudy air, including in-cloud water vapor, could be used to overcome some of the limitations of the RH-based approaches, S89 and D19, and investigate cloud-fraction sensitivity to seeding particles.

Compared to CCT studies using the same model, ECHAM-HAM (Gasparini and Lohmann, 2016; Gasparini et al., 2017, 2020), we found much higher positive net TOA anomalies in response to seeding. ~~For example, Gasparini and Lohmann (2016) followed a globally uniform seeding strategy using particles with radii of $0.5 \mu\text{m}$ and $\tau = 1.05$, like in our study here. In their "Full" cirrus ice nucleation competition simulation (Section 2), they found a positive net anomaly of 0.5 W m^{-2} when seeding with 100 L^{-1} , whereas we found 9.0 W m^{-2} with the same, S89, ice-cloud fraction approach. Results using our updated ice-cloud fraction approach, D19, were also an order of magnitude larger (4.3 W m^{-2}) than those by Gasparini and Lohmann (2016)~~

for the same seeding particle concentration. In addition, our Seed100 results were 16% and 143% larger, for D19 and S89 respectively, than the latest available IPCC forcing estimate of 3.7 Wm^{-2} from a doubling atmospheric CO_2 (Flato et al., 2013; Myhre et al. 790

~~The differences between our results to those by Gasparini and Lohmann (2016) point to~~ This points to differences in the in-situ cirrus scheme (Kärcher et al., 2006, Kuebbeler et al., 2014, Muench and Lohmann 2020, ~~Kärcher and Marcolli 2021~~) and the treatment of ice microphysics (P3: Morrison and Milbrandt 2015, Dietlicher et al., 2018, 2019 versus 2M: Lohmann et al., 795 2007). However, the propensity of heterogeneous nucleation on seeding particles to alter cirrus ice formation in our study is consistent with ongoing research into the complexities of cirrus ice nucleation competition (Lohmann et al., 2008; Mitchell and Finnegan, 2018). In this study we updated the scaling of available aerosols for each freezing mode in the cirrus scheme ~~, excluding dust deposition modes as detailed below,~~ by the fraction of ice in each nucleation mode from the previous timestep out of the total amount of stratiform pre-existing ice (~~Section 2~~Section 2.1). We deem this approach as more accurate than the previous approach to scale the available aerosols by the total amount of pre-existing ice. In a series of tests (not shown) we found that 800 the updated scaling generated more heterogeneously-nucleated ice that only slightly decreased the amount of homogeneously-nucleated ice. The overall impact of the updated scaling did produce more in-situ ice from the cirrus scheme, but did not greatly alter ice nucleation competition. As such, we do not attribute the majority of the differences in our results to previous CCT studies to the scaling changes of available aerosol in each nucleation ~~modes~~mode in the cirrus scheme.

~~We also introduced the new differential activated fraction approach (Kärcher and Marcolli, 2021) with budgeting for the dust deposition modes in the cirrus scheme. This approach no longer overestimates the amount of heterogeneous nucleation via deposition in each cirrus model timestep. Separate sensitivity tests (not shown) showed that this led to more homogeneously nucleated in-situ cirrus ice, inferring a higher efficacy. However, despite some evidence of cooling likely linked to rapid cloud adjustments rather than seeding, our results still differ greatly from those by Gasparini and Lohmann (2016); Gasparini et al. (2017)~~ 810

It is more likely that our results differ ~~to~~from previous CCT studies due to the updated approach to represent ice as a single prognostic category in the microphysics scheme (~~P3, Dietlicher et al., 2018, 2019~~)(P3, Morrison and Milbrandt, 2015; Dietlicher et al., 2018), as opposed to the size-separation approach of in-cloud ice and snow (2M, Lohmann et al., 2007) in earlier versions of the model. The single category approach with P3 is achieved by a prognostic treatment of sedimentation, whereby this process is 815 calculated as a vertical transport tendency based on the total ice ~~particle size distribution (PSD)~~particle size distribution (PSD). Ice removal is represented in a much more realistic way than in the 2M scheme, in which only a part of the ice ~~PSD could fall~~PSD could undergo sedimentation. With the 2M scheme, as soon as ice grows larger than a certain threshold size it is converted to the snow category and falls out of the atmosphere in a single model timestep. In order to maintain realistic cloud IWC values in the 2M scheme compared to observations, ~~and to compensate for the unrealistic ice saturation threshold approach~~ 820 employed by the S89 cloud fraction scheme, ice ice removal via snow formation was artificially enhanced by converting more cloud ice to snow. This was achieved by setting the tuning parameter for snow formation via ice crystal aggregation to an artificially high value ($\gamma_s = 900$, Neubauer et al., 2019; Dietlicher et al., 2019). This is no longer the case with the P3 scheme coupled to D19. A consequence of the slower and more realistic ice removal is that the ice crystal aggregation tuning parameter

is no longer relevant (Table 2, Dietlicher et al., 2019). Instead, ice crystal removal via larger crystals is augmented by an ice
825 self-collection tuning parameter that is set to 6.0 (Section 2.4.5.5 (Section 2.1)). Overall this means that ice in P3 remains in
the atmosphere for a longer period of time. As a result, when seeding particles are introduced as additional INPs with P3, the
more numerous and smaller ~~ice crystals we found~~ ICs (Figure 5 and Figure 6) do not necessarily grow into snow-sized ice
particles and quickly sediment. This explains why we ~~found~~ obtained much higher TOA radiative responses to seeding in this
study compared to ~~Gasparini and Lohmann (2016); Gasparini et al. (2017). We argue, these~~ Gasparini and Lohmann (2016)
830 and Gasparini et al. (2017). These previous CCT studies that did not include a prognostic representation of ice sedimentation
likely underestimated the overseeding response as ice was removed too readily.

Another striking result from our study was the sensitivity of our model to the choice of $S_{i,seed}$. In a separate test, we increased
 $S_{i,seed}$ from 1.05 to 1.35 in an attempt to avoid impacts on heterogeneous nucleation on mineral dust particles, and only target
homogeneous nucleation of liquid sulphate aerosols. Our results to some extent confirmed this hypothesis. 1.35-seeding led
835 to drastic net TOA reductions on a global-scale (Figure 3) and zonally (Figure 9) compared to 1.05-seeding. ~~The cooling we~~
~~found over a broad range of seeding particle concentrations with 1.35-seeding highlights that our model is less sensitive to~~
~~an~~ Despite not finding a significant cooling response, our results showed evidence of a potential "optimal" seeding particle
concentration of $1 L^{-1}$ like Gasparini and Lohmann (2016). More investigation would be required to find an exact optimal
seeding particle concentration ~~like in previous findings (Storelvmo et al., 2013; Gasparini and Lohmann, 2016). This, but this~~
840 is a promising finding as obtaining precise seeding particle concentrations in a potential real-world setting would be difficult that
shows consistency across some CCT studies. The net TOA reductions we found with 1.35-seeding were also confirmed by the
zonal ICNC tracer anomalies (Figure 8). For 1.35-seeding, seeding particles were much less effective at overtaking other
nucleation modes.

~~We found only small regions of negative forcing in both the northern and southern hemispheres for both cases, which to some~~
845 ~~extent compounds our understanding of certain regions being more susceptible to seeding (Storelvmo and Herger, 2014; Storelvmo et al., 2014).~~
~~In the 1.05-seeding case, Seed1 led to a global-mean net reduction of nearly $-0.4 W m^{-2}$. This concentration is similar to~~
~~the optimal seeding concentration found by Gasparini and Lohmann (2016), whose results showed a global net reduction of~~
 ~~$-0.3 W m^{-2}$. However, the total anomalies (Δ) in our model are uncertain in this case, as well as the net response towards high~~
~~latitude regions (Δ). Perhaps a more interesting result is the 1.35-seeding case, where we found noticeable forcing reductions for~~
850 ~~all seeding particle concentrations zonally (Δ). As the Seed10_1.35 net anomaly was the only statistically negative response, we~~
~~examined this case in more detail seasonally in . Based on that analysis, our results do not extend findings by Storelvmo and Herger (2014)~~
~~and Storelvmo et al. (2014) that high-latitude wintertime seeding is an effective strategy. In our model, seeding amplifies the~~
~~already large cirrus in such regions to produce large net warming. Instead, our model points to small regions of summertime~~
~~cooling as a result of seeding, by enhancing the , likely from adjustments in lower-lying mixed-phase and liquid clouds. This~~
855 ~~may be caused by the longer ice residence times within clouds with the scheme, which impacts ice sedimentation into the~~
~~mixed-phase regime. Overall, our results indicate that more thorough investigations of targeted seeding within high-latitude~~
~~regions are needed for future work. Furthermore, our results likely~~ Therefore, our results likely point to a trade-off when pur-
suing further CCT studies: increasing $S_{i,seed}$ is likely an attractive alternative to avoid wide nucleation competition alterations

as seen with lower $S_{i,seed}$, however, the scale to which seeding particles could produce the desired cooling effect remains to be
860 examined with more detailed regional analyses.

~~Our results underscore the need for an investigation into a feasible, instead of using a somewhat arbitrary value as was used in previous studies. Seeding particles were simulated to nucleate ice as a threshold freezing process in our model (Section 2), meaning all aerosol particles within the mode that were available in any given gridbox would nucleate ice upon the right conditions being met. In the 1.05-seeding case this meant that seeding particles would nucleate ice at a relatively low relative
865 to the other nucleation modes, enhancing their ability to overtake other processes and easily produce a strong positive forcing from overseeding (and). The results were less clear in the 1.35-seeding case, with mixed responses throughout the troposphere, which means defining an exact microphysical response is unclear. However, it is clear from our study that the choice of $S_{i,seed}$ is an important factor in determining efficacy. Therefore, more detailed investigations of specific seeding particle materials and their ice-nucleating ability, perhaps in line with the continuous freezing process in this study (Section 2), is also needed in order to
870 move studies in line with potential real-world application.~~

~~Finally, the potential~~ The potential side effects of CCT were only starting to be investigated within the last few years (Lohmann and Gasparini, 2017). In high resolution simulations Gruber et al. (2019) found that CCT not only resulted in thinner cirrus clouds, but also the larger ice particles formed by heterogeneous nucleation on seeding particles acted to reduce lower-lying ~~MPCs~~-MPCs through enhanced riming and ice crystal growth via the WBF process. The combination of these
875 two effects resulted in a net TOA cooling effect. Gasparini et al. (2017) also found an impact on lower-lying clouds in their simulations using an increased sedimentation velocity as a proxy for CCT with seeding particles, following Muri et al. (2014). The "redistribution" of ice to lower-lying MPCs counteracted cooling from reduced cirrus cloud fractions in their sedimentation simulations. In their CCT simulations using seeding INPs, they also found an MPC feedback, resulting from increased convective activity drying the lower troposphere that led smaller MPC fractions. As noted above, our results also showed a
880 sedimentation flux reduction ~~, but we also found in line with~~ a reduction in convective activity due to LW warming by a maximum of ~~roughly 0.7 K/day (not shown)~~ - 0.4 K/day for D19 Seed100, which led to tropospheric stabilization (Figure 12). However, our results do not show significant cloud fraction anomalies in the mixed-phase regime, and rather highlight that the weaker sedimentation flux explains the positive LWC anomaly as shown in Figure 7. MPCs with larger LWC led to stronger SW cooling, ~~which but this~~ was outweighed by warming from the increase of cirrus cloud fractions with smaller and more
885 numerous ICs in the 1.05-seeding case.

Seeding particles were simulated to nucleate ice as a threshold freezing process in our model (Section 2.1), meaning all aerosol particles within the mode that were available in any given gridbox would nucleate ice upon the right conditions being met. This led to the large overseeding responses we found with the lower $S_{i,seed} = 1.05$ that were drastically reduced by increasing $S_{i,seed}$ to 1.35. Based on our findings, it is clear that the choice of $S_{i,seed}$ is an important factor in determining CCT
890 efficacy. Therefore, more detailed investigations of specific seeding particle materials and their ice-nucleating ability, perhaps in line with the continuous freezing process in this study (Section 2.1), are needed in order to move CCT studies in line with potential real-world applications.

895 We also showed that seeding with small particles appears undesirable as they lead to smaller ice particles following nucleation, reduced sedimentation fluxes, and longer-lived cirrus clouds. Gasparini et al. (2017) found seeding with larger particles to lead to larger cooling that can somewhat offset CO₂-induced warming.

900 Finally, the timing of seeding particle injection is also key so as to only seed regions prior to natural cirrus formation. This poses one of the largest uncertainties for CCT, as forecasting cirrus formation is difficult with current techniques. In addition, predicting where cirrus ice forms predominantly via homogeneous nucleation will be a significant challenge. Studies like those by Storelvmo and Herger (2014), Storelvmo et al. (2014), and Gruber et al. (2019) suggest that high-latitude, wintertime seeding is optimal primarily due to the lack of cirrus SW CRE during this period (i.e. cirrus only act in the LW spectrum via warming). In addition, higher latitude regions on average contain lower background aerosol concentrations, making them more ideal for homogeneous nucleation within cirrus. Our results do not confirm high-latitude wintertime seeding as an effective strategy, as we found that seeding amplifies the already large cirrus LW CRE in such regions for most cases to produce net TOA warming. Overall, our results indicate that more thorough investigations of targeted seeding within high latitude regions are needed for future work. This could be partially addressed with more high resolution studies using cloud-resolving models, like Gruber et al. (2019). On the other hand, further CCT studies using GCMs can address this issue by using a more complex, non-uniform approach to include seeding particles as INPs for cirrus ice nucleation competition. This is the subject of further investigation in our group.

910 The results presented in this study underscore the need to investigate the methods in which seeding particles are included as INPs within models. We propose three topics in which future work should focus: (1) a dedicated seeding particle parameterization that accounts for the mechanism of ice formation on seeding particles and feasible $S_{i,seed}$ values, instead of using a somewhat arbitrary value as was used in CCT studies to date, (2) an optimal seeding particle size, and (3) the spatial and temporal distribution of seeding particles in models.

5 Conclusions

915 We tested the sensitivity of CCT efficacy to the approach used for calculating ice cloud fractions and $S_{i,seed}$ using a the new physically-based ~~representation of ice microphysics~~ P3 ice microphysics scheme in the ECHAM-HAM GCM (Dietlicher et al., 2018, 2019). We conclude with the following main findings:

1. Increasing the RH ~~thresholds~~ threshold for the calculation of cirrus cloud fractions τ reduces the positive forcing from overseeding by avoiding artificial cirrus cloud expansion upon ice nucleation.
 - 920 2. The ~~more realistic,~~ prognostic treatment of sedimentation ~~with in~~ the P3 microphysics scheme, leading to ~~much slower ice removal than with the~~ slower and more physically-based ice removal, is likely the reason why we find such large seeding responses compared to the study by Gasparini and Lohmann (2016), using the default ECHAM 2M ~~scheme as in Gasparini and Lohmann (2016), likely means that responses to seeding are no longer underestimated. Rather, seeding in our scheme.~~ Our model produces smaller and more numerous ice particles that amplify the already longer ice residence times within clouds to induce a strong positive TOA forcing.
- 925

3. Increasing $S_{i,seed}$ ~~from 1.05 to 1.35 eliminates overseeding~~, ~~indicating a broad range of seeding particle concentrations that increase the likelihood of producing a cooling response~~reduces the large overseeding found with the lower $S_{i,seed}$ of 1.05, with evidence of an "optimal" seeding particle concentration that is consistent with previous CCT studies using the same model (Gasparini and Lohmann, 2016).
- 930 4. Globally CCT is unlikely to produce the desired cooling effects due to dynamic adjustments and background aerosol concentration heterogeneity. Instead, small regions centered around specific latitudes show only a small potential of targeted seeding.
5. Our results do not ~~support~~confirm that wintertime high-latitude seeding ~~;~~contrasting can optimize CCT ~~efficacy,~~contrasting the results obtained by Storelvmo and Herger (2014) and Storelvmo et al. (2014). ~~We found small regions of cooling in the summer hemisphere that likely led to feedbacks on lower-lying mixed-phase clouds, arguing that~~Thus, targeted seeding for specific regions or time periods should be further investigated in higher resolution modeling studies like the one by Gruber et al. (2019).
- 935

~~The results presented in this study make a good case for testing the sensitivity of different seeding particle parameterizations. We showed that increasing can lead to drastically different outcomes, limiting the potential for warming from overseeding. We also showed that seeding with small particles appears undesirable as they lead to smaller ice particles following nucleation, reduced sedimentation fluxes, and longer-lived cirrus clouds. Gasparini et al. (2017) found seeding with larger particles to lead to larger cooling that can somewhat offset CO₂-induced warming. In addition, the timing of seeding particle injection is key so as to only seed regions prior to natural cirrus formation. This poses one of the largest uncertainties for, as forecasting cirrus formation is difficult with current techniques. On top of that, predicting where cirrus ice forms predominantly via homogeneous nucleation will be a significant challenge.~~

940

945

~~Arguably, the abandonment of the size-dependent hydrometeor class separation approach with can make the interpretation of seeding impacts closer to first principles (Dietlicher et al., 2018). However, there~~There are still large differences in the outcome of CCT studies between the two leading climate models that ~~to date~~at the time of writing were used to study CCT, ECHAM-HAM and CESM-CAM (Storelvmo et al., 2014; Penner et al., 2015; Gasparini and Lohmann, 2016; Gasparini et al., 2017), ~~regardless of a new ice microphysics scheme.~~ Such wide differences can be partially attributed to a lack of reliable in-situ observations of cirrus in order to constrain models, though this gap is starting to be closed with more recent studies (Krämer et al., 2016; Krämer et al., 2020). ~~However, our results also~~Our results instead extend the conclusion that a consistent CCT approach among climate modeling groups ~~on studies~~ is needed (Gasparini et al., 2020), especially if the desire amongst the scientific community is to critically assess this proposed method as a feasible climate intervention strategy.

950

955 In line with the proposed real-world delivery mechanism of seeding particles using commercial aircraft (Mitchell and Finnegan, 2009), there is a need to test the impact of aviation soot emissions on cirrus formation by including soot particles as potential INPs within the cirrus regime (e.g., Lohmann et al., 2020). Following on from that analysis, designing future CCT studies to include aviation will more closely align modelling studies to potential implementation.

Appendix A: Orographic cirrus verification

960 In this section we verify our approach to not include orographic effects on vertical velocity in our model, using the P3 ice
microphysics scheme. We ran an additional reference simulation with the D19 setup with the orographic velocity enhancement
parameterization by Joos et al. (2008, 2010) activated (ORO). Here we compare the Full_D19 (REF) with ORO with spatial
distributions of ICNC and in-situ ice number tracers.

Figure A1 presents the spatial distributions of ICNC per temperature bin from 203 K to 233 K for the ten-year mean
965 DARDAR observations (a-c), and for the five-year mean model predictions for REF (d-f) and ORO (g-i). Our model shows
much wider ICNC variation than the DARDAR data for all temperature bins presented here. Krämer et al. (2020) provide
several reasons that explain the differences between the ICNC of these two observation platforms. Most notably is that
DARDAR cannot detect the low ICNC associated with aged thin cirrus clouds at cold temperatures that were observed
in the in-situ measurements. This is primarily due to the assumptions made in the retrieval algorithm that is based on the
970 parameterization by Delanoë et al. (2005) on particle size distribution (PSD) parameter constraints. As Sourdeval et al. (2018)
note, this parameterization does not necessarily capture the multi-modality of the ice PSD observed in the in-situ measurements
they compared in their study. This culminates in a potential over-prediction of small ICs associated with high ICNC values at
low temperatures that Krämer et al. (2020) explain is due to the transient nature of homogeneous nucleation and the complexities
in observing this process in in-situ field campaigns. This is compounded by the fact that lidar and radar measurements are not
975 always available simultaneously (Sourdeval et al., 2018).

Mountainous regions such as the Himalayas, the Andes, and the Rockies are already evident with local ICNC maxima in
our REF simulation for all three temperature bins (Figure A1d-f). By adding the orographic velocity component, ICNC spatial
heterogeneity is reduced, leading to much higher ICNC over wider areas. We argue this over-predicts high ICNC values and
leads to additional warming.

980 The competition between homogeneous and heterogeneous nucleation in in-situ cirrus is highly uncertain (Cziczo et al., 2013; Krämer et
al., 2020). As the number of ICs following a homogeneous nucleation event is highly dependent on the vertical velocity that determines
the degree of ice supersaturation (Jensen et al., 2016b), it follows that accounting for vertical velocity variability by including
orographic enhancement is requisite. Gasparini and Lohmann (2016), who also used the ECHAM-HAM GCM, showed that
even with the orographic parameterization by Joos et al. (2008, 2010) that the dominant source of cirrus ICs at 200 hPa was
985 through heterogeneous nucleation (see their Figure 3). In our model the opposite is the case (Figure A2). Homogeneously-nucleated
ice outweighs heterogeneously-nucleated ice in REF, and is only enhanced further when including the orographic velocity
component such that spatial heterogeneity is also reduced. This is due the difference between the default ECHAM-HAM
microphysics scheme by Lohmann et al. (2007) (2M) and the new P3 scheme (Dietlicher et al., 2018, 2019). With the prognostic
sedimentation employed in the latter, leading to slower ice removal, smaller ICs remain in the atmosphere for longer periods
990 than in 2M. Therefore, we argue, that while the enhancement of homogeneous nucleation was required in the model with the
2M scheme, it is no longer required when using the P3 scheme as homogeneous nucleation is not underpredicted relative to
in-situ cirrus ice nucleation competition.

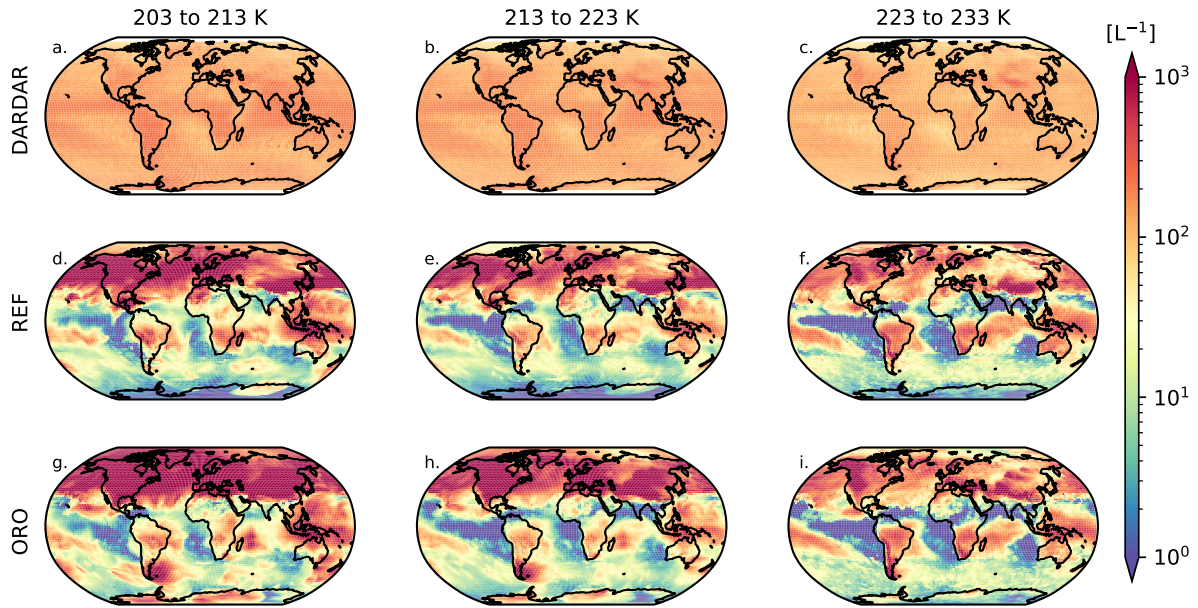


Figure A1. Spatial distributions of ICNC in L^{-1} per DARDAR-defined 10 K temperature bin for (a-c) 2006-2016 mean DARDAR ICNC $> 5 \mu m$ (Sourdeval et al., 2018), and five-year annual mean model ICNC for (d-f) REF (Full D19 setup per the main text) with no orographic effects, and (g-i) ORO with active orographic effects.

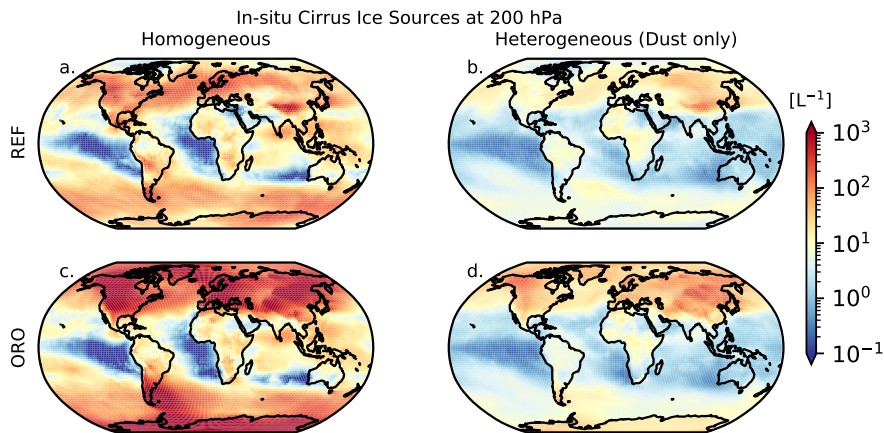


Figure A2. Five-year annual mean spatial distributions of in-situ ice number tracers in L^{-1} at 200 hPa for (a-b) REF (Full D19 setup per the main text) without orographic effects, and (c-d) ORO with orographic effects active. The first column shows the distribution of the in-situ homogeneously nucleated ice number and the second column shows the total in-situ heterogeneously nucleated ice number, which includes dust only as these are non-seeding simulations.

Code and data availability. The data for this study are available online at: <https://doi.org/10.5281/zenodo.6344980> (Tully et al., 2022a). The scripts used for post-processing the raw output data and producing the figures for this manuscript are available online at:
995 <https://doi.org/10.5281/zenodo.6346856> (Tully et al., 2022b). In-situ measurement data were provided directly by Martina Krämer (m.kraemer@fz-juelich.de) as well as the DARDAR satellite data by Ordan Sourdeval (odran.sourdeval@univ-lille.fr)

Author contributions. Colin Tully, David Neubauer and Ulrike Lohmann designed the experiments. Colin Tully ran the model simulations, analysed the data, post-processing and plotting, and wrote the manuscript with comments from all co-authors. Nadja Omanovic contributed to the model development and the data analysis. Ulrike Lohmann and David Neubauer helped with the interpretation of the results.

1000 *Competing interests.* The authors declare that they have no conflict of interest.

Acknowledgements. This Project is funded by the European Union under the Grant Agreement No. ~~875036~~-[875036 \(ACACIA\)](#). This work was supported by a grant from the Swiss National Supercomputing Centre (CSCS) under project ID s903. The authors would like to thank Martina Krämer for graciously providing the in-situ measurement data for model validation, Jörg Wieder for invaluable Python help to prepare the figures for this manuscript, Sylvaine Ferrachat for technical assistance running the model and analysing the data, Bernat Jiménez Esteve for providing helpful advice for interpreting our results for discussion of stratospheric impacts, and Steffen Münch for helping to understand the cirrus scheme and for fruitful discussions on seeding particle implementation potential within the model. [Finally, we would like to thank the reviewers of this manuscript for taking time to provide useful feedback for improving this study.](#)

References

- Butchart, N.: The Brewer-Dobson circulation, *Reviews of Geophysics*, 52, 157–184, <https://doi.org/10.1002/2013RG000448>, <https://agupubs.onlinelibrary.wiley.com/doi/abs/10.1002/2013RG000448>, 2014.
- 1010 Butchart, N. and Scafe, A.: Removal of chlorofluorocarbons by increased mass exchange between the stratosphere and troposphere in a changing climate, *Nature*, 410, 799–802, <https://doi.org/https://doi.org/10.1038/35071047>, <https://www.nature.com/articles/35071047>, 2001.
- Butchart, N., Scafe, A., Bourqui, M., de Grandpré, J., Hare, S., Kettleborough, J., Langematz, U., Manzini, E., Sassi, F., Shibata, K., Shindell, D., and Sigmond, M.: Simulations of anthropogenic change in the strength of the Brewer–Dobson circulation, *Climate Dynamics*, 27, 727–741, <https://doi.org/10.1007/s00382-006-0162-4>, <https://doi.org/10.1007/s00382-006-0162-4>, 2006.
- 1015 Calvo, N., Garcia, R. R., Randel, W. J., and Marsh, D. R.: Dynamical Mechanism for the Increase in Tropical Upwelling in the Lowermost Tropical Stratosphere during Warm ENSO Events, *Journal of the Atmospheric Sciences*, 67, 2331–2340, <https://doi.org/10.1175/2010JAS3433.1>, <https://journals.ametsoc.org/view/journals/atsc/67/7/2010jas3433.1.xml>, 2010.
- 1020 Crutzen, P. J.: Albedo Enhancement by Stratospheric Sulfur Injections: A Contribution to Resolve a Policy Dilemma?, *Climatic Change*, 77, 2784–2786, <https://doi.org/10.1007/s10584-006-9101-y>, <https://doi.org/10.1007/s10584-006-9101-y>, 2006.
- Cziczo, D. J., Froyd, K. D., Hoose, C., Jensen, E. J., Diao, M., Zondlo, M. A., Smith, J. B., Twohy, C. H., and Murphy, D. M.: Clarifying the Dominant Sources and Mechanisms of Cirrus Cloud Formation, *Science*, 340, 1320–1324, <https://doi.org/10.1126/science.1234145>, <https://science.sciencemag.org/content/340/6138/1320>, 2013.
- 1025 Cziczo, D. J., Wolf, M. J., Gasparini, B., Münch, S., and Lohmann, U.: Unanticipated Side Effects of Stratospheric Albedo Modification Proposals Due to Aerosol Composition and Phase, *Scientific Reports*, 9, <https://doi.org/10.1038/s41598-019-53595-3>, <https://doi.org/10.1038/s41598-019-53595-3>, 2019.
- Delanoë, J., Protat, A., Testud, J., Bouniol, D., Heymsfield, A. J., Bansemer, A., Brown, P. R. A., and Forbes, R. M.: Statistical properties of the normalized ice particle size distribution, *Journal of Geophysical Research: Atmospheres*, 110, <https://doi.org/https://doi.org/10.1029/2004JD005405>, <https://agupubs.onlinelibrary.wiley.com/doi/abs/10.1029/2004JD005405>, 2005.
- 1030 DeMott, P. J., Cziczo, D. J., Prenni, A. J., Murphy, D. M., Kreidenweis, S. M., Thomson, D. S., Borys, R., and Rogers, D. C.: Measurements of the concentration and composition of nuclei for cirrus formation, *Proceedings of the National Academy of Sciences*, 100, 14 655–14 660, <https://doi.org/10.1073/pnas.2532677100>, <https://www.pnas.org/content/100/25/14655>, 2003.
- DeMott, P. J., Prenni, A. J., Liu, X., Kreidenweis, S. M., Petters, M. D., Twohy, C. H., Richardson, M. S., Eidhammer, T., and Rogers, D. C.: Predicting global atmospheric ice nuclei distributions and their impacts on climate, *Proceedings of the National Academy of Sciences*, 107, 11 217–11 222, <https://doi.org/10.1073/pnas.0910818107>, <https://www.pnas.org/content/107/25/11217>, 2010.
- 1035 Dietlicher, R., Neubauer, D., and Lohmann, U.: Prognostic parameterization of cloud ice with a single category in the aerosol-climate model ECHAM(v6.3.0)-HAM(v2.3), *Geoscientific Model Development*, 11, 1557–1576, <https://doi.org/10.5194/gmd-11-1557-2018>, <https://gmd.copernicus.org/articles/11/1557/2018/>, 2018.
- 1040 Dietlicher, R., Neubauer, D., and Lohmann, U.: Elucidating ice formation pathways in the aerosol–climate model ECHAM6-HAM2, *Atmospheric Chemistry and Physics*, 19, 9061–9080, <https://doi.org/10.5194/acp-19-9061-2019>, <https://www.atmos-chem-phys.net/19/9061/2019/>, 2019.

- Dykema, J. A., Keith, D. W., and Keutsch, F. N.: Improved aerosol radiative properties as a foundation for solar geoengineering risk assessment, *Geophysical Research Letters*, 43, 7758–7766, <https://doi.org/https://doi.org/10.1002/2016GL069258>, <https://agupubs.onlinelibrary.wiley.com/doi/abs/10.1002/2016GL069258>, 2016.
- 1045 Flato, G., J., Marotzke, B., Abiodun, P., Braconnot, S., Chou, W., Collins, P., Cox, F., Driouech, S., Emori, V., Eyring, C., Forest, P., Gleckler, E., Guilyardi, C., Jakob, V., Kattsov, C., Reason, and Rummukainen, M.: Evaluation of Climate Models, Cambridge University Press, <https://doi.org/10.1017/CBO9781107415324.020>, 2013.
- Gasparini, B. and Lohmann, U.: Why cirrus cloud seeding cannot substantially cool the planet, *Journal of Geophysical Research: Atmospheres*, 121, 4877–4893, <https://doi.org/10.1002/2015JD024666>, <https://agupubs.onlinelibrary.wiley.com/doi/abs/10.1002/2015JD024666>, 2016.
- 1050 Gasparini, B., Münch, S., Poncet, L., Feldmann, M., and Lohmann, U.: Is increasing ice crystal sedimentation velocity in geoengineering simulations a good proxy for cirrus cloud seeding?, *Atmospheric Chemistry and Physics*, 17, 4871–4885, <https://doi.org/10.5194/acp-17-4871-2017>, <https://acp.copernicus.org/articles/17/4871/2017/>, 2017.
- 1055 Gasparini, B., Meyer, A., Neubauer, D., Münch, S., and Lohmann, U.: Cirrus Cloud Properties as Seen by the CALIPSO Satellite and ECHAM-HAM Global Climate Model, *Journal of Climate*, 31, 1983–2003, <https://doi.org/10.1175/JCLI-D-16-0608.1>, <https://doi.org/10.1175/JCLI-D-16-0608.1>, 2018.
- Gasparini, B., McGraw, Z., Storelmo, T., and Lohmann, U.: To what extent can cirrus cloud seeding counteract global warming?, *Environmental Research Letters*, 15, 054002, <https://doi.org/10.1088/1748-9326/ab71a3>, <https://doi.org/10.1088%2F1748-9326%2Fab71a3>, 2020.
- 1060 Gruber, S., Blahak, U., Haenel, F., Kottmeier, C., Leisner, T., Muskatel, H., Storelmo, T., and Vogel, B.: A Process Study on Thinning of Arctic Winter Cirrus Clouds With High-Resolution ICON-ART Simulations, *Journal of Geophysical Research: Atmospheres*, 124, 5860–5888, <https://doi.org/10.1029/2018JD029815>, <https://agupubs.onlinelibrary.wiley.com/doi/abs/10.1029/2018JD029815>, 2019.
- Gryspeerd, E., Sourdeval, O., Quaas, J., Delanoë, J., Krämer, M., and Kühne, P.: Ice crystal number concentration estimates from lidar–radar satellite remote sensing – Part 2: Controls on the ice crystal number concentration, *Atmospheric Chemistry and Physics*, 18, 14351–14370, <https://doi.org/10.5194/acp-18-14351-2018>, <https://acp.copernicus.org/articles/18/14351/2018/>, 2018.
- 1065 Heymsfield, A. J., Krämer, M., Luebke, A., Brown, P., Cziczo, D. J., Franklin, C., Lawson, P., Lohmann, U., McFarquhar, G., Ulanowski, Z., and Van Tricht, K.: Cirrus Clouds, *Meteorological Monographs*, 58, 2.1–2.26, <https://doi.org/10.1175/AMSMONOGRAPHIS-D-16-0010.1>, <https://doi.org/10.1175/AMSMONOGRAPHIS-D-16-0010.1>, 2017.
- 1070 Hoesly, R. M., Smith, S. J., Feng, L., Klimont, Z., Janssens-Maenhout, G., Pitkanen, T., Seibert, J. J., Vu, L., Andres, R. J., Bolt, R. M., Bond, T. C., Dawidowski, L., Kholod, N., Kurokawa, J.-I., Li, M., Liu, L., Lu, Z., Moura, M. C. P., O’Rourke, P. R., and Zhang, Q.: Historical (1750–2014) anthropogenic emissions of reactive gases and aerosols from the Community Emissions Data System (CEDS), *Geoscientific Model Development*, 11, 369–408, <https://doi.org/10.5194/gmd-11-369-2018>, <https://gmd.copernicus.org/articles/11/369/2018/>, 2018.
- Hong, Y., Liu, G., and Li, J.-L. F.: Assessing the Radiative Effects of Global Ice Clouds Based on CloudSat and CALIPSO Measurements, *Journal of Climate*, 29, 7651 – 7674, <https://doi.org/10.1175/JCLI-D-15-0799.1>, <https://journals.ametsoc.org/view/journals/clim/29/21/jcli-d-15-0799.1.xml>, 2016.
- 1075 Ickes, L., Welti, A., Hoose, C., and Lohmann, U.: Classical nucleation theory of homogeneous freezing of water: thermodynamic and kinetic parameters, *Phys. Chem. Chem. Phys.*, 17, 5514–5537, <https://doi.org/10.1039/C4CP04184D>, <http://dx.doi.org/10.1039/C4CP04184D>, 2015.

- 1080 Jensen, E. J., Ueyama, R., Pfister, L., Bui, T. V., Alexander, M. J., Podglajen, A., Hertzog, A., Woods, S., Lawson, R. P., Kim, J.-E., and Schoeberl, M. R.: High-frequency gravity waves and homogeneous ice nucleation in tropical tropopause layer cirrus, *Geophysical Research Letters*, 43, 6629–6635, <https://doi.org/10.1002/2016GL069426>, <https://agupubs.onlinelibrary.wiley.com/doi/abs/10.1002/2016GL069426>, 2016a.
- Jensen, E. J., Ueyama, R., Pfister, L., Bui, T. V., Lawson, R. P., Woods, S., Thornberry, T., Rollins, A. W., Diskin, G. S., DiGangi, J. P.,
1085 and Avery, M. A.: On the Susceptibility of Cold Tropical Cirrus to Ice Nuclei Abundance, *Journal of the Atmospheric Sciences*, 73, 2445–2464, <https://doi.org/10.1175/JAS-D-15-0274.1>, <https://doi.org/10.1175/JAS-D-15-0274.1>, 2016b.
- Joos, H., Spichtinger, P., Lohmann, U., Gayet, J.-F., and Minikin, A.: Orographic cirrus in the global climate model ECHAM5, *Journal of Geophysical Research: Atmospheres*, 113, <https://doi.org/https://doi.org/10.1029/2007JD009605>, <https://agupubs.onlinelibrary.wiley.com/doi/abs/10.1029/2007JD009605>, 2008.
- 1090 Joos, H., Spichtinger, P., and Lohmann, U.: Influence of a future climate on the microphysical and optical properties of orographic cirrus clouds in ECHAM5, *Journal of Geophysical Research: Atmospheres*, 115, <https://doi.org/https://doi.org/10.1029/2010JD013824>, <https://agupubs.onlinelibrary.wiley.com/doi/abs/10.1029/2010JD013824>, 2010.
- Kanji, Z. A., Ladino, L. A., Wex, H., Boose, Y., Burkert-Kohn, M., Cziczo, D. J., and Krämer, M.: Overview of Ice Nucleating Particles, *Meteorological Monographs*, 58, 1.1–1.33, <https://doi.org/10.1175/AMSMONOGRAPHIS-D-16-0006.1>, <https://doi.org/10.1175/AMSMONOGRAPHIS-D-16-0006.1>, 2017.
- 1095 Keith, D. W., Weisenstein, D. K., Dykema, J. A., and Keutsch, F. N.: Stratospheric solar geoengineering without ozone loss, *Proceedings of the National Academy of Sciences*, 113, 14 910–14 914, <https://doi.org/10.1073/pnas.1615572113>, <https://www.pnas.org/content/113/52/14910>, 2016.
- Koop, T., Luo, B., Tsias, A., and Peter, T.: Water activity as the determinant for homogeneous ice nucleation in aqueous solutions, *Nature*,
1100 406, 611–614, <https://doi.org/10.1038/35020537>, 2000.
- Krämer, M., Rolf, C., Luebke, A., Afchine, A., Spelten, N., Costa, A., Meyer, J., Zöger, M., Smith, J., Herman, R. L., Buchholz, B., Ebert, V., Baumgardner, D., Borrmann, S., Klingebiel, M., and Avallone, L.: A microphysics guide to cirrus clouds – Part 1: Cirrus types, *Atmospheric Chemistry and Physics*, 16, 3463–3483, <https://doi.org/10.5194/acp-16-3463-2016>, <https://acp.copernicus.org/articles/16/3463/2016/>, 2016.
- 1105 Krämer, M., Rolf, C., Spelten, N., Afchine, A., Fahey, D., Jensen, E., Khaykin, S., Kuhn, T., Lawson, P., Lykov, A., Pan, L. L., Riese, M., Rollins, A., Stroh, F., Thornberry, T., Wolf, V., Woods, S., Spichtinger, P., Quaas, J., and Sourdeval, O.: A microphysics guide to cirrus – Part 2: Climatologies of clouds and humidity from observations, *Atmospheric Chemistry and Physics*, 20, 12 569–12 608, <https://doi.org/10.5194/acp-20-12569-2020>, <https://acp.copernicus.org/articles/20/12569/2020/>, 2020.
- Kuebbeler, M., Lohmann, U., and Feichter, J.: Effects of stratospheric sulfate aerosol geo-engineering on cirrus clouds, *Geophysical Research Letters*, 39, <https://doi.org/https://doi.org/10.1029/2012GL053797>, <https://agupubs.onlinelibrary.wiley.com/doi/abs/10.1029/2012GL053797>, 2012.
- 1110 Kuebbeler, M., Lohmann, U., Hendricks, J., and Kärcher, B.: Dust ice nuclei effects on cirrus clouds, *Atmospheric Chemistry and Physics*, 14, 3027–3046, <https://doi.org/10.5194/acp-14-3027-2014>, <https://www.atmos-chem-phys.net/14/3027/2014/>, 2014.
- Kärcher, B. and Burkhardt, U.: A cirrus cloud scheme for general circulation models, *Quarterly Journal of the Royal Meteorological Society*,
1115 134, 1439–1461, <https://doi.org/https://doi.org/10.1002/qj.301>, <https://rmets.onlinelibrary.wiley.com/doi/abs/10.1002/qj.301>, 2008.

- Kärcher, B. and Lohmann, U.: A parameterization of cirrus cloud formation: Homogeneous freezing of supercooled aerosols, *Journal of Geophysical Research: Atmospheres*, 107, AAC 4–1–AAC 4–10, <https://doi.org/10.1029/2001JD000470>, <https://agupubs.onlinelibrary.wiley.com/doi/abs/10.1029/2001JD000470>, 2002.
- 1120 Kärcher, B. and Lohmann, U.: A parameterization of cirrus cloud formation: Heterogeneous freezing, *Journal of Geophysical Research: Atmospheres*, 108, <https://doi.org/10.1029/2002JD003220>, <https://agupubs.onlinelibrary.wiley.com/doi/abs/10.1029/2002JD003220>, 2003.
- Kärcher, B. and Marcolli, C.: Aerosol-cloud interactions: The representation of heterogeneous ice activation in cloud models, *Atmospheric Chemistry and Physics Discussions*, 2021, 1–11, <https://doi.org/10.5194/acp-2021-511>, <https://acp.copernicus.org/preprints/acp-2021-511/>, 2021.
- 1125 Kärcher, B., Hendricks, J., and Lohmann, U.: Physically based parameterization of cirrus cloud formation for use in global atmospheric models, *Journal of Geophysical Research: Atmospheres*, 111, <https://doi.org/10.1029/2005JD006219>, <https://agupubs.onlinelibrary.wiley.com/doi/abs/10.1029/2005JD006219>, 2006.
- Kärcher, B., DeMott, P. J., Jensen, E. J., and Harrington, J. Y.: Studies on the Competition Between Homogeneous and Heterogeneous Ice Nucleation in Cirrus Formation, *Journal of Geophysical Research: Atmospheres*, 127, e2021JD035805, <https://doi.org/https://doi.org/10.1029/2021JD035805>, <https://agupubs.onlinelibrary.wiley.com/doi/abs/10.1029/2021JD035805>, e2021JD035805 2021JD035805, 2022.
- 1130 Levkov, L., Rockel, B., Kapitzka, H., and Raschke, E.: 3D mesoscale numerical studies of cirrus and stratus clouds by their time and space evolution, *Contributions to atmospheric physics*, 65, 35–58, 1992.
- Lohmann, U. and Diehl, K.: Sensitivity Studies of the Importance of Dust Ice Nuclei for the Indirect Aerosol Effect on Stratiform Mixed-Phase Clouds, *Journal of the Atmospheric Sciences*, 63, 968–982, <https://doi.org/10.1175/JAS3662.1>, <https://doi.org/10.1175/JAS3662.1>, 1135 2006.
- Lohmann, U. and Ferrachat, S.: Impact of parametric uncertainties on the present-day climate and on the anthropogenic aerosol effect, *Atmospheric Chemistry and Physics*, 10, 11 373–11 383, <https://doi.org/10.5194/acp-10-11373-2010>, <https://acp.copernicus.org/articles/10/11373/2010/>, 2010.
- Lohmann, U. and Gasparini, B.: A cirrus cloud climate dial?, *Science*, 357, 248–249, <https://doi.org/10.1126/science.aan3325>, <https://science.sciencemag.org/content/357/6348/248>, 2017.
- 1140 Lohmann, U. and Kärcher, B.: First interactive simulations of cirrus clouds formed by homogeneous freezing in the ECHAM general circulation model, *Journal of Geophysical Research: Atmospheres*, 107, AAC 8–1–AAC 8–13, <https://doi.org/10.1029/2001JD000767>, <https://agupubs.onlinelibrary.wiley.com/doi/abs/10.1029/2001JD000767>, 2002.
- Lohmann, U., Stier, P., Hoose, C., Ferrachat, S., Kloster, S., Roeckner, E., and Zhang, J.: Cloud microphysics and aerosol indirect effects in the global climate model ECHAM5-HAM, *Atmospheric Chemistry and Physics*, 7, 3425–3446, <https://doi.org/10.5194/acp-7-3425-2007>, <https://www.atmos-chem-phys.net/7/3425/2007/>, 2007.
- 1145 Lohmann, U., Spichtinger, P., Jess, S., Peter, T., and Smit, H.: Cirrus cloud formation and ice supersaturated regions in a global climate model, *Environmental Research Letters*, 3, 045 022, <https://doi.org/10.1088/1748-9326/3/4/045022>, <https://doi.org/10.1088%2F1748-9326%2F3%2F4%2F045022>, 2008.
- 1150 Lohmann, U., Lüönd, F., and Mahrt, F.: An Introduction to Clouds: From the Microscale to Climate, Cambridge University Press, <https://doi.org/10.1017/CBO9781139087513>, 2016.
- Lohmann, U., Friebel, F., Kanji, Z., Mahrt, F., Mensah, A., and Neubauer, D.: Future warming exacerbated by aged-soot effect on cloud formation, *Nature Geoscience*, 13, 674–680, <https://doi.org/10.1038/s41561-020-0631-0>, <https://doi.org/10.1038/s41561-020-0631-0>, 2020.

- 1155 Mahrt, F., Marcolli, C., David, R. O., Grönquist, P., Barthazy Meier, E. J., Lohmann, U., and Kanji, Z. A.: Ice nucleation abilities of soot particles determined with the Horizontal Ice Nucleation Chamber, *Atmospheric Chemistry and Physics*, 18, 13 363–13 392, <https://doi.org/10.5194/acp-18-13363-2018>, <https://acp.copernicus.org/articles/18/13363/2018/>, 2018.
- 1160 Mahrt, F., Kilchhofer, K., Marcolli, C., Grönquist, P., David, R. O., Rösch, M., Lohmann, U., and Kanji, Z. A.: The Impact of Cloud Processing on the Ice Nucleation Abilities of Soot Particles at Cirrus Temperatures, *Journal of Geophysical Research: Atmospheres*, 125, e2019JD030 922, <https://doi.org/10.1029/2019JD030922>, <https://agupubs.onlinelibrary.wiley.com/doi/abs/10.1029/2019JD030922>, e2019JD030922 10.1029/2019JD030922, 2020.
- Mauritsen, T., Stevens, B., Roeckner, E., Crueger, T., Esch, M., Giorgetta, M., Haak, H., Jungclaus, J., Klocke, D., Matei, D., Mikolajewicz, U., Notz, D., Pincus, R., Schmidt, H., and Tomassini, L.: Tuning the climate of a global model, *Journal of Advances in Modeling Earth Systems*, 4, <https://doi.org/https://doi.org/10.1029/2012MS000154>, <https://agupubs.onlinelibrary.wiley.com/doi/abs/10.1029/2012MS000154>, 2012.
- 1165 Mitchell, D. L. and Finnegan, W.: Modification of cirrus clouds to reduce global warming, *Environmental Research Letters*, 4, 045 102, <https://doi.org/10.1088/1748-9326/4/4/045102>, <https://doi.org/10.1088%2F1748-9326%2F42F4%2F045102>, 2009.
- Mitchell, D. L., Rasch, P., Ivanova, D., McFarquhar, G., and Nousiainen, T.: Impact of small ice crystal assumptions on ice sedimentation rates in cirrus clouds and GCM simulations, *Geophysical Research Letters*, 35, <https://doi.org/https://doi.org/10.1029/2008GL033552>, <https://agupubs.onlinelibrary.wiley.com/doi/abs/10.1029/2008GL033552>, 2008.
- 1170 Möhler, O., Field, P. R., Connolly, P., Benz, S., Saathoff, H., Schnaiter, M., Wagner, R., Cotton, R., Krämer, M., Mangold, A., and Heymsfield, A. J.: Efficiency of the deposition mode ice nucleation on mineral dust particles, *Atmospheric Chemistry and Physics*, 6, 3007–3021, <https://doi.org/10.5194/acp-6-3007-2006>, <https://acp.copernicus.org/articles/6/3007/2006/>, 2006.
- Morrison, H. and Milbrandt, J. A.: Parameterization of Cloud Microphysics Based on the Prediction of Bulk Ice Particle Properties. Part I: Scheme Description and Idealized Tests, *Journal of the Atmospheric Sciences*, 72, 287–311, <https://doi.org/10.1175/JAS-D-14-0065.1>, <https://doi.org/10.1175/JAS-D-14-0065.1>, 2015.
- 1175 Muench, S. and Lohmann, U.: Developing a Cloud Scheme With Prognostic Cloud Fraction and Two Moment Microphysics for ECHAM-HAM, *Journal of Advances in Modeling Earth Systems*, 12, e2019MS001 824, <https://doi.org/10.1029/2019MS001824>, <https://agupubs.onlinelibrary.wiley.com/doi/abs/10.1029/2019MS001824>, e2019MS001824 2019MS001824, 2020.
- Muri, H., Kristjánsson, J. E., Storelmo, T., and Pfeffer, M. A.: The climatic effects of modifying cirrus clouds in a climate engineering framework, *Journal of Geophysical Research: Atmospheres*, 119, 4174–4191, <https://doi.org/10.1002/2013JD021063>, <https://agupubs.onlinelibrary.wiley.com/doi/abs/10.1002/2013JD021063>, 2014.
- 1180 Murphy, D. M.: Effect of Stratospheric Aerosols on Direct Sunlight and Implications for Concentrating Solar Power, *Environ. Sci. Technol.*, 43, 2784–2786, <https://doi.org/10.1021/es802206b>, <https://doi.org/10.1021/es802206b>, 2009.
- Murray, B. J., O’Sullivan, D., Atkinson, J. D., and Webb, M. E.: Ice nucleation by particles immersed in supercooled cloud droplets, *Chem. Soc. Rev.*, 41, 6519–6554, <https://doi.org/10.1039/C2CS35200A>, <http://dx.doi.org/10.1039/C2CS35200A>, 2012.
- Myhre, G., Myhre, C. L., Forster, P. M., and Shine, K. P.: Halfway to doubling of CO₂ radiative forcing, *Nature Geoscience*, 10, 710–711, <https://doi.org/10.1038/ngeo3036>, <https://doi.org/10.1038/ngeo3036>, 2017.
- 1190 Möhler, O., Benz, S., Saathoff, H., Schnaiter, M., Wagner, R., Schneider, J., Walter, S., Ebert, V., and Wagner, S.: The effect of organic coating on the heterogeneous ice nucleation efficiency of mineral dust aerosols, *Environmental Research Letters*, 3, 025 007, <https://doi.org/10.1088/1748-9326/3/2/025007>, <https://doi.org/10.1088/1748-9326/3/2/025007>, 2008.

- Neubauer, D., Lohmann, U., Hoose, C., and Frontoso, M. G.: Impact of the representation of marine stratocumulus clouds on the anthropogenic aerosol effect, *Atmospheric Chemistry and Physics*, 14, 11 997–12 022, <https://doi.org/10.5194/acp-14-11997-2014>, <https://www.atmos-chem-phys.net/14/11997/2014/>, 2014.
- 1195 Neubauer, D., Ferrachat, S., Siegenthaler-Le Drian, C., Stier, P., Partridge, D. G., Tegen, I., Bey, I., Stanelle, T., Kokkola, H., and Lohmann, U.: The global aerosol–climate model ECHAM6.3–HAM2.3 – Part 2: Cloud evaluation, aerosol radiative forcing, and climate sensitivity, *Geoscientific Model Development*, 12, 3609–3639, <https://doi.org/10.5194/gmd-12-3609-2019>, <https://gmd.copernicus.org/articles/12/3609/2019/>, 2019.
- Pelucchi, P., Neubauer, D., and Lohmann, U.: Vertical grid refinement for stratocumulus clouds in the radiation scheme of the global climate model ECHAM6.3–HAM2.3–P3, *Geoscientific Model Development*, 14, 5413–5434, <https://doi.org/10.5194/gmd-14-5413-2021>, <https://gmd.copernicus.org/articles/14/5413/2021/>, 2021.
- 1200 Penner, J. E., Zhou, C., and Liu, X.: Can cirrus cloud seeding be used for geoengineering?, *Geophysical Research Letters*, 42, 8775–8782, <https://doi.org/10.1002/2015GL065992>, <https://agupubs.onlinelibrary.wiley.com/doi/abs/10.1002/2015GL065992>, 2015.
- Possner, A., Ekman, A. M. L., and Lohmann, U.: Cloud response and feedback processes in stratiform mixed-phase clouds perturbed by ship exhaust, *Geophysical Research Letters*, 44, 1964–1972, <https://doi.org/https://doi.org/10.1002/2016GL071358>, <https://agupubs.onlinelibrary.wiley.com/doi/abs/10.1002/2016GL071358>, 2017.
- 1205 Rind, D. and Lonergan, P.: Modeled impacts of stratospheric ozone and water vapor perturbations with implications for high-speed civil transport aircraft, *Journal of Geophysical Research: Atmospheres*, 100, 7381–7396, <https://doi.org/https://doi.org/10.1029/95JD00196>, <https://agupubs.onlinelibrary.wiley.com/doi/abs/10.1029/95JD00196>, 1995.
- Rind, D., Lerner, J., and McLinden, C.: Changes of tracer distributions in the doubled CO₂ climate, *Journal of Geophysical Research: Atmospheres*, 106, 28 061–28 079, <https://doi.org/https://doi.org/10.1029/2001JD000439>, <https://agupubs.onlinelibrary.wiley.com/doi/abs/10.1029/2001JD000439>, 2001.
- 1210 Robock, A.: Volcanic eruptions and climate, *Reviews of Geophysics*, 38, 191–219, <https://doi.org/https://doi.org/10.1029/1998RG000054>, <https://agupubs.onlinelibrary.wiley.com/doi/abs/10.1029/1998RG000054>, 2000.
- Robock, A., Jerch, K., and Bunzl, M.: 20 reasons why geoengineering may be a bad idea, *Bulletin of the Atomic Scientists*, 64, 14–59, <https://doi.org/10.1080/00963402.2008.11461140>, <https://doi.org/10.1080/00963402.2008.11461140>, 2008.
- 1215 Sourdeval, O., Gryspeerdt, E., Krämer, M., Goren, T., Delanoë, J., Afchine, A., Hemmer, F., and Quaas, J.: Ice crystal number concentration estimates from lidar–radar satellite remote sensing – Part 1: Method and evaluation, *Atmospheric Chemistry and Physics*, 18, 14 327–14 350, <https://doi.org/10.5194/acp-18-14327-2018>, <https://acp.copernicus.org/articles/18/14327/2018/>, 2018.
- Spichtinger, P. and Cziczo, D. J.: Impact of heterogeneous ice nuclei on homogeneous freezing events in cirrus clouds, *Journal of Geophysical Research: Atmospheres*, 115, <https://doi.org/https://doi.org/10.1029/2009JD012168>, <https://agupubs.onlinelibrary.wiley.com/doi/abs/10.1029/2009JD012168>, 2010.
- 1220 Stephens, G. L., Tsay, S.-C., Stackhouse, P. W., and Flatau, P. J.: The Relevance of the Microphysical and Radiative Properties of Cirrus Clouds to Climate and Climatic Feedback, *Journal of Atmospheric Sciences*, 47, 1742 – 1754, [https://doi.org/10.1175/1520-0469\(1990\)047<1742:TROTMA>2.0.CO;2](https://doi.org/10.1175/1520-0469(1990)047<1742:TROTMA>2.0.CO;2), https://journals.ametsoc.org/view/journals/atsc/47/14/1520-0469_1990_047_1742_trotma_2_0_co_2.xml, 1990.
- 1225 Stevens, B., Giorgetta, M., Esch, M., Mauritsen, T., Crueger, T., Rast, S., Salzmann, M., Schmidt, H., Bader, J., Block, K., Brokopf, R., Fast, I., Kinne, S., Kornbluh, L., Lohmann, U., Pincus, R., Reichler, T., and Roeckner, E.: Atmospheric component of the MPI-M

- Earth System Model: ECHAM6, *Journal of Advances in Modeling Earth Systems*, 5, 146–172, <https://doi.org/10.1002/jame.20015>, <https://agupubs.onlinelibrary.wiley.com/doi/abs/10.1002/jame.20015>, 2013.
- 1230 Stier, P., Feichter, J., Kinne, S., Kloster, S., Vignati, E., Wilson, J., Ganzeveld, L., Tegen, I., Werner, M., Balkanski, Y., Schulz, M., Boucher, O., Minikin, A., and Petzold, A.: The aerosol-climate model ECHAM5-HAM, *Atmospheric Chemistry and Physics*, 5, 1125–1156, <https://doi.org/10.5194/acp-5-1125-2005>, <https://www.atmos-chem-phys.net/5/1125/2005/>, 2005.
- Storelvmo, T. and Herger, N.: Cirrus cloud susceptibility to the injection of ice nuclei in the upper troposphere, *Journal of Geophysical Research: Atmospheres*, 119, 2375–2389, <https://doi.org/10.1002/2013JD020816>, [https://agupubs.onlinelibrary.wiley.com/doi/abs/10.1002/](https://agupubs.onlinelibrary.wiley.com/doi/abs/10.1002/2013JD020816)
 1235 2013JD020816, 2014.
- Storelvmo, T., Kristjánsson, J. E., Muri, H., Pfeffer, M., Barahona, D., and Nenes, A.: Cirrus cloud seeding has potential to cool climate, *Geophysical Research Letters*, 40, 178–182, <https://doi.org/10.1029/2012GL054201>, <https://agupubs.onlinelibrary.wiley.com/doi/abs/10.1029/2012GL054201>, 2013.
- Storelvmo, T., Boos, W. R., and Herger, N.: Cirrus cloud seeding: a climate engineering mechanism with reduced side effects?, *Philosophical Transactions of the Royal Society A: Mathematical, Physical and Engineering Sciences*, 372, 20140116, <https://doi.org/10.1098/rsta.2014.0116>, <https://royalsocietypublishing.org/doi/abs/10.1098/rsta.2014.0116>, 2014.
- Sundqvist, H., Berge, E., and Kristjánsson, J. E.: Condensation and Cloud Parameterization Studies with a Mesoscale Numerical Weather Prediction Model, *Monthly Weather Review*, 117, 1641–1657, [https://doi.org/10.1175/1520-0493\(1989\)117<1641:CACPSW>2.0.CO;2](https://doi.org/10.1175/1520-0493(1989)117<1641:CACPSW>2.0.CO;2), [https://doi.org/10.1175/1520-0493\(1989\)117<1641:CACPSW>2.0.CO;2](https://doi.org/10.1175/1520-0493(1989)117<1641:CACPSW>2.0.CO;2), 1989.
- 1245 Tegen, I., Neubauer, D., Ferrachat, S., Siegenthaler-Le Drian, C., Bey, I., Schutgens, N., Stier, P., Watson-Parris, D., Stanelle, T., Schmidt, H., Rast, S., Kokkola, H., Schultz, M., Schroeder, S., Daskalakis, N., Barthel, S., Heinold, B., and Lohmann, U.: The global aerosol-climate model ECHAM6.3-HAM2.3 – Part 1: Aerosol evaluation, *Geoscientific Model Development*, 12, 1643–1677, <https://doi.org/10.5194/gmd-12-1643-2019>, <https://gmd.copernicus.org/articles/12/1643/2019/>, 2019.
- Tully, C., Neubauer, D., Omanovic, N., and Lohmann, U.: Data for the "Cirrus cloud thinning using a more physically-based ice microphysics scheme in the ECHAM-HAM GCM" manuscript, <https://doi.org/10.5281/zenodo.6344980>, <https://doi.org/10.5281/zenodo.6344980>, 2022a.
- 1250 Tully, C., Neubauer, D., Omanovic, N., and Lohmann, U.: Data analysis and plotting scripts for the "Cirrus cloud thinning using a more physically-based ice microphysics scheme in the ECHAM-HAM GCM" manuscript, <https://doi.org/10.5281/zenodo.6346856>, <https://doi.org/10.5281/zenodo.6346856>, working version at the moment., 2022b.
- 1255 Ullrich, R., Hoose, C., M?hler, O., Niemand, M., Wagner, R., H?hler, K., Hiranuma, N., Saathoff, H., and Leisner, T.: A New Ice Nucleation Active Site Parameterization for Desert Dust and Soot, *Journal of the Atmospheric Sciences*, 74, 699 – 717, <https://doi.org/10.1175/JAS-D-16-0074.1>, <https://journals.ametsoc.org/view/journals/atasc/74/3/jas-d-16-0074.1.xml>, 2017.
- van Marle, M. J. E., Kloster, S., Magi, B. I., Marlon, J. R., Danianu, A.-L., Field, R. D., Arneth, A., Forrest, M., Hantson, S., Kehrwald, N. M., Knorr, W., Lasslop, G., Li, F., Mangeon, S., Yue, C., Kaiser, J. W., and van der Werf, G. R.: Historic global biomass burning emissions for
 1260 CMIP6 (BB4CMIP) based on merging satellite observations with proxies and fire models (1750–2015), *Geoscientific Model Development*, 10, 3329–3357, <https://doi.org/10.5194/gmd-10-3329-2017>, <https://gmd.copernicus.org/articles/10/3329/2017/>, 2017.
- Vaughan, N. E. and Lenton, T. M.: A review of climate geoengineering proposals, *Climate Change*, 109, 745–790, <https://doi.org/10.1007/s10584-011-0027-7>, <https://doi.org/10.1007/s10584-011-0027-7>, 2011.
- Villanueva, D., Neubauer, D., Gasparini, B., Ickes, L., and Tegen, I.: Constraining the Impact of Dust-Driven Droplet
 1265 Freezing on Climate Using Cloud-Top-Phase Observations, *Geophysical Research Letters*, 48, e2021GL092687,

<https://doi.org/https://doi.org/10.1029/2021GL092687>, <https://agupubs.onlinelibrary.wiley.com/doi/abs/10.1029/2021GL092687>,
e2021GL092687 2021GL092687, 2021.

1270 Wilks, D. S.: “The Stippling Shows Statistically Significant Grid Points”: How Research Results are Routinely Overstated and Overinterpreted, and What to Do about It, *Bulletin of the American Meteorological Society*, 97, 2263 – 2273, <https://doi.org/10.1175/BAMS-D-15-00267.1>, <https://journals.ametsoc.org/view/journals/bams/97/12/bams-d-15-00267.1.xml>, 2016.

Zhang, K., O’Donnell, D., Kazil, J., Stier, P., Kinne, S., Lohmann, U., Ferrachat, S., Croft, B., Quaas, J., Wan, H., Rast, S., and Feichter, J.: The global aerosol-climate model ECHAM-HAM, version 2: sensitivity to improvements in process representations, *Atmospheric Chemistry and Physics*, 12, 8911–8949, <https://doi.org/10.5194/acp-12-8911-2012>, <https://www.atmos-chem-phys.net/12/8911/2012/>, 2012.